SANDIA REPORT
SAND2008-6490
Unlimited Release
Printed December 2008

Improved Power Source for Doubling the Exchange Time Interval of LLC

LDRD Funded Project

Ganesan Nagasubramanian

Prepared by
Sandia National Laboratories
Albuquerque, New Mexico 87185

Sandia is a multi-program laboratory operated by Sandia Corporation,
a Lockheed Martin Company, for the United States Department of Energy's
National Nuclear Security Administration under Contract DE-AC04-94AL85000.

Issued by Sandia National Laboratories, operated for the United States Department of Energy by Sandia Corporation.

Available to DOE and DOE contractors from
U.S. Department of Energy
Office of Scientific and Technical Information
P.O. Box 62
Oak Ridge, TN 37831

Telephone: (865) 576-8401
Facsimile: (865) 576-5728
E-Mail: reports@adonis.osti.gov
Online ordering: http://www.osti.gov/bridge

Available to the public from
U.S. Department of Commerce
National Technical Information Service
5285 Port Royal Rd.
Springfield, VA 22161

Telephone: (800) 553-6847
Facsimile: (703) 605-6900
E-Mail: orders@ntis.fedworld.gov
Online order: http://www.ntis.gov/help/ordermethods.asp?loc=7-4-0#online

SAND2008-6490
Unlimited Release
Printed December 2008

Improved Power Source for Doubling the Exchange Time Interval of LLC

LDRD Funded Project

Ganesan Nagasubramanian
Sandia National Laboratories
Advanced Power Sources R&D Dept. 2546
P.O. Box 5800
Albuquerque, NM 87185-0614

Abstract

This LDRD project attempts to use novel electrochemical techniques to understand the reaction mechanism that limits the discharge reaction of lithium CF_x chemistry. If this advanced component development and exploratory investigations efforts are successful we will have a High Energy Density Li Primary Battery Technology with the capability to double the run time in the same volume, or provide the same energy in a much smaller volume. These achievements would be a substantial improvement over commercial Li/Thionyl chloride battery technology.

The $Li(CF_x)_n$ chemistry has the highest theoretical energy (and capacity) and hence very attractive for long life battery applications. However, the practical open circuit voltage (OCV) is only 3.2 V which is ~1.3 V lower than the thermodynamic cell voltage (for an in depth explanation of the voltage depression refer to "Introduction" below). The presence of intermediate has been invoked to explain the lower OCV of the cell. Due to the reduction in cell voltage the cell out put is reduced by ~40%.

To account for the initial voltage loss a mechanism has been proposed which involves the formation of a ternary compound (like $C(LiF)_x$). But neither its presence nor its nature has been confirmed. Our work will seek to develop understanding of the voltage depression with a goal to produce a primary battery with improved properties that will have significant impact in furthering advancements.

Acknowledgment

I would like to thank Kevin Zavadil (Org 1825) for performing high resolution interfacial studies and Lorie Davis for making electrodes, building and testing cells. The author would also like to thank Mark Rodriguez (Org 1822) for performing in-situ x-ray studies. Additionally, I thank Mark and Mike Keenan (Org 1822) for performing Multivariate Analyses on the x-ray data and extracting evidence for the presence of the intermediate in the discharge reaction of $(CF_x)_n$. Finally, I would like to thank Joanne Budzien (Org 1814) for performing Molecular Dynamic Simulation model and Professor Wolverton and Dr. Shin of Northwestern University for performing the Density Functional Theory model in search for the intermediate in the discharge reaction of $(CF_x)_n$.

Contents

Figures

Tables

Acronyms and Abbreviations

AFM	Atomic Force Microscopy
Ahr	Ampere Hour (unit of capacity of a battery)
$(CF_x)_n$	Carbon Monofluoride
cP	Centipoise (unit of viscosity)
F-NMR	Fluorine Nuclear Magnetic Resonance
Kg	Kilogram
kJ	Kilo Joules (Energy)
L	Liter
LDRD	Laboratory Directed Research and Development
Li	Lithium
LLC	Limited Life Component
mA	milli-Ampere
mil	0.001 inch
MVA	Multivariate Analysis
OCV	Open circuit Voltage
PVDF	Polyvinylidene Di-fluoride
STM	Scanning Tunneling Microscopy
TOF SIMS	Time of Flight Secondary Ion Mass Spectroscopy
W	Watt (Power)
Whr	Watt Hour (Energy)

Executive Summary

Purpose

The work documented in this report was undertaken for one key purpose:

> To understand the mechanism of the discharge reaction of Li/$(CF_x)_n$ cell to improve the operating voltage and thus double the exchange time interval of the LLC.

Accomplishments:

Key Results and Conclusions:

1. Fabricated (CF_x) electrodes with uniform loading and reproducible performance.

2. Performed *in-situ* x-ray on Li/(CF_x) pouch cells while discharging cell.

3. Applied Multivariate Analysis and identified existence of intermediate in the discharge reaction. This is a major accomplishment.

4. Three papers have been published in international refereed journals.

   - G. Nagasubramanian, M. Rodriguez, "Performance Enhancement at Low Temperatures and in-situ X-ray Analyses of Discharge Reaction of Li/$(CF_x)_n$ Cells, J. Power Sources 170, 179-184(2007)
   - M. Rodriguez, M. R. Keenan and G. Nagasubramanian, "In-situ X-ray Analyses of $(CF_x)_n$ Battery: Signal Extraction by Multivariate Analysis, J. Applied Crystallography 40, 1097-1104(2007)
   - *Ganesan Nagasubramanian, "***Fabrication and Testing Capabilities for 18650 Li/(CFx)n Cells"** *Int. J. Electrochem. Sci.,* 2, 913 – 922(2007)

5. Employed two different models to identify the nature of the intermediate. The two models include: 1) Molecular Dynamics Simulations: This simulation will provide atomistic detail about the reactions that occur including the products, reactants, and intermediate compounds. Simulation is able to observe small changes in stoichiometry and chemical bonds. 2) Density Functional Theory: Computationally search for what types of intermediate compounds might form electrochemically during this discharge reaction, and also where they are in the overall voltage curve. Hopefully, then that understanding might help us to suggest chemistries or processing routes that would avoid this intermediate.

   Both these models suggest the presence of intermediate in the discharge reaction.

1. Introduction

Lithium ambient temperature primary batteries are being proposed and developed as power sources for surety applications such as code control and Permissive Action Link (PAL) or Code Management Systems (CMS). These batteries will be limited life components (LLCs) in this type of use and must have high reliability, predictable aging characteristics, and make maximum use of available space to meet minimum lifetime requirements under all environments. It would be highly desirable to develop advanced power sources with the capability to last more than a minimum LLC exchange interval without sacrificing any reliability, safety or power performance. This cannot be done with existing technology. Lifetime in the application is directly governed by the deliverable energy/capacity that can be obtained from a specific volume.

Lithium batteries have high theoretical energy density, although the practical energy is typically much lower than the theoretical. All batteries deliver less than theoretical capacity/energy for several reasons. One reason for this is the burden from inactive cell and battery packaging materials that can add considerable weight and volume. This can vary depending on the containment needs of the particular cell materials. Additional losses in delivered capacity can result from depression in operating voltage from the theoretical, or from inherent features of the cell electrochemistry, such as increasing internal resistance during discharge, increases resulting from cold temperature. These issues can be dealt with to improve the percentage of theoretical energy/capacity that is actually delivered for use. However, the central issue in the case of CFx is voltage loss which lowers the cell output by ~40%. The facts that cell potential losses are observed immediately upon discharging a cell and remain nearly constant over a range of discharge conditions and times have been used to argue that an interface controlled by a specific graphite intercalated compound (or GIC) or ternary intermediate results in lost function. A definitive determination of the existence of a GIC layer and an understanding of its characteristics (i.e. composition, structure thickness) is required in order to identify strategies for tailoring its properties and improving the cell output.

In the (CFx) chemistry, if the discharge reaction proceeds via the reaction scheme given below the OCV of the battery should be around 4.5 V. This mechanism assumes that the overall reaction (C) is a direct reaction between Li^+ and F^-. The theoretical specific energy for the CF_x (with x=1) chemistry will then be ~3900 Whr/kg. This is obtained by multiplying the thermodynamic cell voltage of 4.5 V and the capacity per unit weight of 865 Ahr/kg. This calculation assumes a simple reaction mechanism between the Li and CF_x to C and LiF.

Description of cell chemistry:
The overall reaction for the Li-CF_x chemistry is given below:

$$x\ Li \text{ ------ } x\ Li^+ + x\ e^- \quad \text{(anode reaction)} \qquad (A)$$

$$x\ e^- + CF_x \text{ ----- } C + F_x^- \quad \text{(cathode reaction)} \qquad (B)$$

$$x\ Li^+ + C + F_x^- \text{ ---- } x\ LiF + C \quad \text{(overall reaction)} \qquad (C)$$

The overall reaction involves the generation of carbon and the formation and precipitation of LiF in the cathode pores. In addition to high theoretical energy density, this chemistry is inherently safe, exhibits long life and is extremely thermally stable. The chemistry has not been fully optimized to deliver maximum energy. Currently CF_x cells are being used in memory backup applications where the cell is discharged at a very low current. However, surety applications requirements include increasing delivered energy, so as to be able to increase the run time of the device. Thus, the aim of this project is to increase the delivered energy of the CF_x cells at a moderate rate and improve performance at sub-ambient temperatures so that these inherently safe and stable cells can be used in long life surety applications for NW. Demonstration of a long-life (10 yr) cell concept is needed within the next 5 years.

Although, the thermodynamic OCV is ~4.5 V, the observed OCV is around 3.2 V. Further, upon discharge at a moderate rate, the operating voltage of the cell goes down to ~2.6 V which is a lot lower than the 4.5 V computed from thermodynamic considerations. This reduction in voltage decreases the practical energy significantly. The practical energy is around 2249 Whr/kg (2800 Wh/L). This value was computed by multiplying the operating voltage of ~2.6 V and 865 Ahr/kg.

The important question that needs to be answered is "why the measured OCV is 3.2 V and not 4.5 V?" unlike in other primary Li primary chemistries where the practical OCV is at or close to thermodynamic OCV. For example, in the case of lithium thionyl chloride ($Li\text{-}SOCl_2$) the measured OCV of 3.65 V is equal to the voltage predicted by the thermodynamic computation.

The reason for the precipitous drop in OCV for CFx is not apparent but implies that perhaps the reaction mechanism is not as straight forward as described above. A new discharge reaction mechanism that accounts for the OCV depression has been proposed and is shown below.

Anode Reaction: $Li + zPC \longrightarrow Li^+.zPC + e^-$ ------(1)

Cathode Reaction: $(CF) + Li^+.zPC + e \longrightarrow C\text{-}F\text{-}Li.zPC$ -----(2)

Total Reaction:

$$(CF)_n + mLi + mzPC \longrightarrow (CF)_{n-m} + m(C\text{-}F\text{-}Li.zPC) \quad \text{------(3)}$$

$$\downarrow$$

$$mC + mLiF + mzPC \quad \text{------(4)}$$

This reaction scheme invokes the formation of a ternary intermediate (reaction step #2) which decomposes to the final product. This advanced reaction mechanism suggests that as soon as the cell is fabricated/activated the solvated Li^+ reacts instantly with the cathode forming a solvated ternary compound. Based on this supposition Touhara et al came up with a free energy flow chart to account for the formation of the ternary intermediate and subsequent decomposition to the end products (shown in Figure 1 below). In this model calculation the authors have taken propylene carbonate (PC) as the solvent. To account for the OCV depression to 3.2 V the formation of a ternary compound (C-F---Li.zPC) by electrochemical reaction has been hypothesized. Subsequently, the intermediate chemically decomposes to yet another compound ($C+F^-.zPC+Li^+.zPC$) which finally desolvates to C + LiF + zPC.

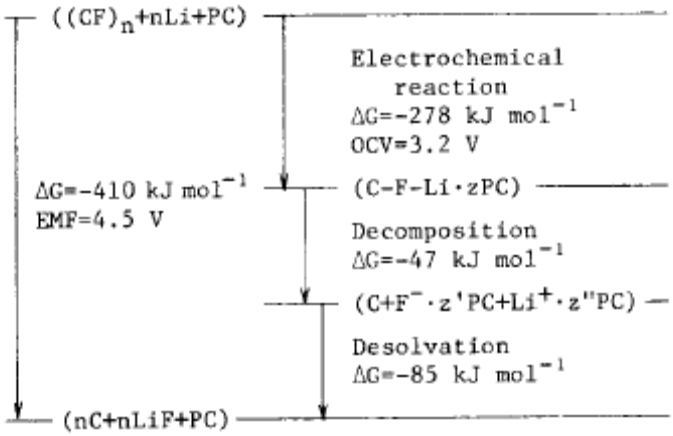

Figure 1. Relative position of each reaction state in free energy during the discharge of $Li/(CF_x)_n$ Cell.

(Reproduced from H. Touhara, H. Fujimoto, N. Watanabe and A. Tressaud, Solid State Ionics, 14, 163(1984) with permission from Elsevier).

While this reaction scheme suggests the existence of the ternary intermediate there is no direct proof or indirect evidence for its existence. So the principal objective of this LDRD is to search first for the existence of the intermediate and second characterize the nature of the intermediate. Once the nature of the intermediate is known, technical solutions may then be proposed for improving the operating voltage of the cell and thus to improve the discharge energy. We took a step by step approach which aims first to detect the presence of the intermediate by in-situ x-ray measurement and second to identify the nature of the intermediate by modeling.

Additionally, we also performed a series of spectroscopic probes with electrochemical scanning tunneling microscopy to locally and systematically form and probe the advancing interfacial region in a series of graphite-derived carbon monofluoride materials. The new aspect of the research we are proposing is to locally discharge the intercalated cathode in a systematic fashion and monitor the resulting changes in structural and conductive properties. This experiment was conducted on an electrochemical scanning tunneling microscope. These measurements are true in situ measurements conducted in real time using propylene carbonate and or other organic electrolytes. The imaging tip is also used to drive local discharge allowing for a progressive picture to evolve of local structural changes as a function of time (discharge duration at constant rate) or current density (discharge rate as at constant time). From such experiments, we identify the characteristics of and learn the relative kinetics of events like graphene sheet delamination, GIC interphase formation, and LiF nanocrystalite nucleation and growth.

A second novel aspect will be the generation of electrode designed for individual particle analysis using a combination of techniques beyond STM. Graphite-based CFx will be our starting material in powder form. Powders will be sized produce monodispersed particle populations. Solution-based assembly onto either suitable planar electrodes or transmission electron microscopy (TEM) grids will be employed eliminating the need for embedding particles in a conductive matrix. Similar concepts have been used to orient carbon nanotubes *end-on* onto

planar substrates for device fabrication. The grid concept allows for controlled atmosphere extraction of a STM interrogated electrode to conduct secondary structural and compositional analysis. Time-of-flight secondary ion mass spectrometry will be used in a 3-dimensional imaging mode to determine both the GIC thickness and composition. Larger particles of > 10 micron will be the subject of SIMS analysis. We have developed multivariate spectral analysis that is particularly useful for separating out spatially correlated chemical signatures. This aspect of Sandia's unique approach to SIMS provides a method of discriminating between the GIC and precipitated LiF. SIMS has sub-nanometer depth sensitivity allowing for a determination of GIC layer thickness. TEM technique will also be applied for chemical and structural characterization. Selected area diffraction can provide extremely high spatial resolution required for the GIC interphase, well beyond the limits encountered in x-ray techniques. Electron energy loss spectroscopy conducted on the TEM will provide quantitative compositional information.

The product of these research activities will be the development of a single particle platform and the techniques necessary to establish structure-property relationships at the single micron sized particle level. Our focus will be on understanding fundamental mechanisms and charting strategies for overcoming voltage depression in CFx for future application in weapon system as power source.

The accomplishments in the electrochemical, in-situ x-ray and spectroscopic studies are described below. The first segment describes the electrochemical, in-situ x-ray and electrode fabrication studies. The second segment describes accomplishments that relates to the use of surface chemistry tools such as STM, AFM etc.

2. Activities for FY06-FY08

2.1 FY-06----1st Year

It is imperative that we have good quality electrode for testing and evaluation. In FY06 we developed in-house capability to coat large electrodes. We made several $(CF_x)_n$ electrodes with PVDF (Polyvinylene difluoride) as binder. To my knowledge we are the first to coat $(CF_x)_n$ electrodes with PVDF as binder. A photo of the Sandia National Laboratories coated electrode is shown in Figure 2.

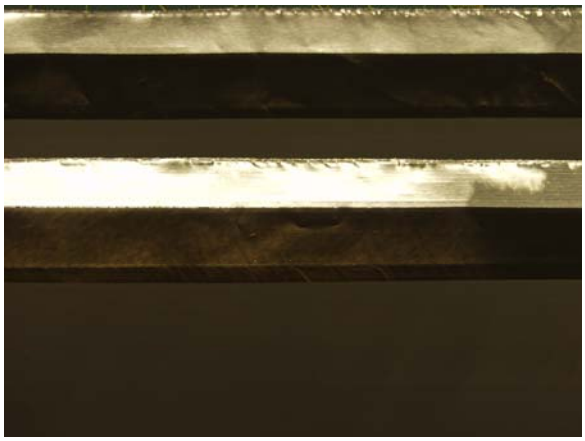

Figure 2. SNL Coated CF_x Electrode.

Typical composition of $(CF_x)_n$ electrode:

90 w% $(CF_x)_n$; 5 w% Shawingin Acetalyne Black (Honeywell); 5 w% PVDF (Kureha W#1300). Electrode thickness: ~2.5 mil. A detailed description of the electrode making and coating is given later in this report.

Using our electrode coater (SNL in-house capability has been published in *Int. J. Electrochem. Sci.,* 2 (**2007)** 913 – 922 (Appendix A)) we coated $(CF)_n$ electrodes of uniform thickness and loading. We evaluated them in coin cells for performance at different temperatures in the range of 72 to -55°C. Our test data clearly showed that the SNL cells had improved performance over the commercial cells of comparable size and were highly reproducible. We also made large capacity cells (18650-type) and tested them for capacity at high temperature. Typically these cells gave >3 Ahr capacity.

In FY06 we initiated a contract to the University of South Carolina (USC) for modeling (based on first principle) cell performance at different temperatures and rates. This model will also have "predictive" capability which will eliminate making measurements at conditions that are not easily obtainable in the laboratory. In FY06 we also collected discharge data on commercial cells to support the modeling activity.

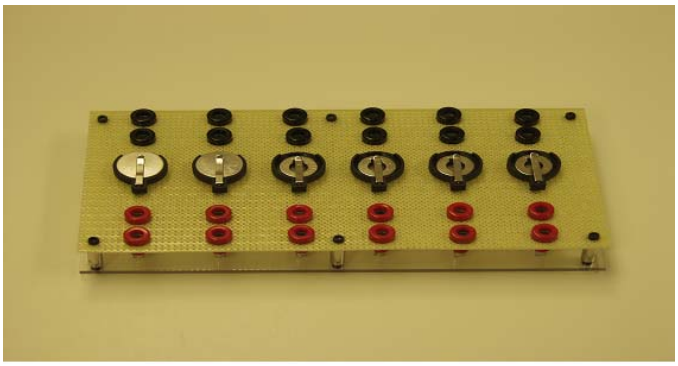

Figure 3. Coin Cell Holder.

During the electrode coating studies we realized that $(CF_x)_n$ needs a thin coating (~ 3 micron) of conductive carbon on aluminum substrate for improved adhesion. I obtained carbon-coated (2-3 micron thick) aluminum electrodes from Intelicoat a small company located in South Hadley, MA. In a typical run 7.5 grams of PVDF is added to 200 ml of NMP (1-Methy-2- pyrrolidinone) to 800 grams of Zirconia beads and the mixture is stirred for 15 minutes to dissolve the PVDF. To this solution are added 7.5 grams of conductive carbon and stir again for 20 more minutes. Finally add 135 grams of (CF_x)n powder to the above mixture and stir at 3200 RPM for 1 hr. The time was found to be sufficient to homogenize the mixture to consistent slurry of viscosity in the range 220-250 cP. This slurry was then coated on to aluminum substrate obtained from Intelicoat. These electrodes were used for the electrochemical studies.

2.1.1 Coin Cell Testing

In the cell holder (Figure 3 above) we can test a maximum of 6 coin cells at a time. The cells were tested in Moccor tester at temperature. Since these are primary cells they cannot be recharged. Typically these cells gave around 10 mAhr capacity. A typical discharge curve is shown in Figure 2. The open circuit voltage is around 3.4 V. The operating voltage is around 2.6 V even for a low discharge rate (C/100).

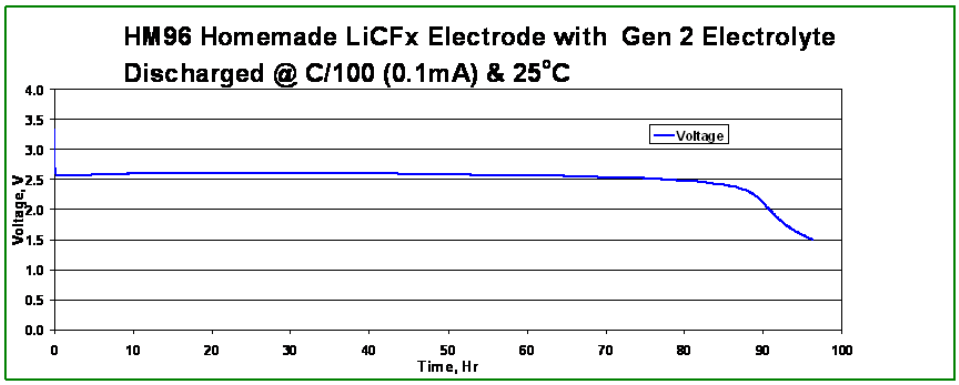

Figure 4. Discharge Behavior of a SNL Made Coin Cell.

2.1.2 X-ray studies

Further, we performed in-situ x-ray diffraction measurement studies on Sandia built pouch cells while the cell is discharging to gather structural data on changes in the cathode material or the appearance of crystalline discharge products. We have shown that a pouch cell configuration can be used to perform *in-situ* x-ray studies to obtain structural information of the cathode during discharge. It took us several trial runs and iterations to hit the right thickness of the plastic bag (that contains the cell components) to maximize signal from the $(CF_x)_n$ electrode. Sample configuration of the test pouch cell is given below (Figure 5). The grey side is where a very thin (~2.2 mil) Li anode is located.

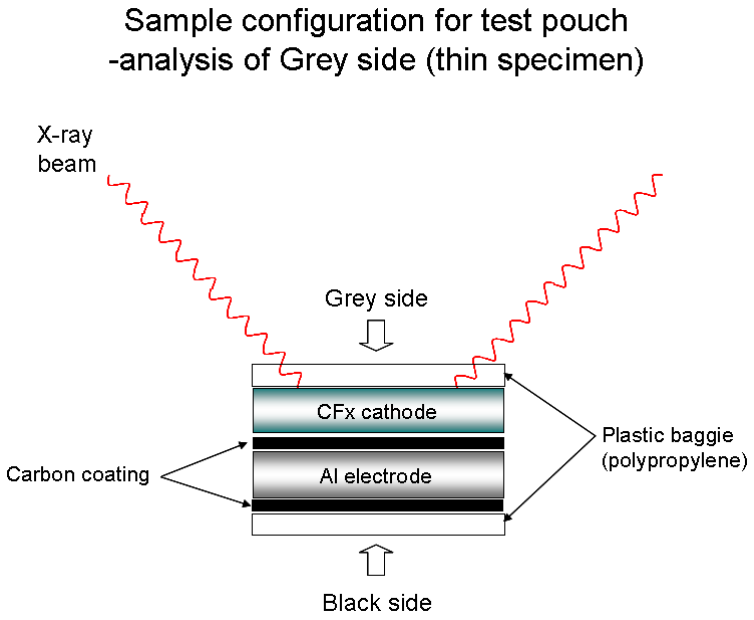

Figure 5. Sample Configuration for In-situ X-ray.

We used the cell configuration shown above to collect in-situ x-ray data on $(CF_x)_n$ cells while the cell is discharging. This study has the potential to yield information of any intermediate species (that is X-ray detectable) formed in the discharge reaction sequence. We collected a series of x-ray data on the cell while discharging and the presence of the intermediate was not apparent in the x-ray data. We used SNLs' unique modeling capability to extract information on the intermediate from the x-ray data. We performed Multivariate Analysis on this data and extracted information on the presence of the intermediate. The analysis was performed in FY07 and will be discussed later.

Additionally, we also performed in-situ measurements (described below) for understanding the interfacial reaction at the electrolyte/CFx interface and nature of the intermediate.

2.1.3 In-situ TEM and other studies

FY06 activities are focused on developing the capability to conduct isolated cathodic discharge and characterization on single particles of carbon monofluoride. Initial efforts are focused on fixing single particles to suitable substrates and demonstrating the probing of these particles. Emphasis has been placed on scanning probe microscopy, initially as an ex situ probe, but with the intent of conducting in situ imaging during local cathodic discharge. A preliminary demonstration of single particle compositional characterization is also conducted using time-of-flight secondary ion mass spectrometry (TOF SIMS). Particles have been fixed to amorphous carbon TEM grids with the intent of analytical electron microscopy and diffraction on individual particles.

The basic orientation of particles presented to the electrolyte during discharge is shown in Figure 6 for a Sandia fabricated CF_x cathode. A suspension of CF_x, carbon black, and binder is dispersed onto a carbon coated Al foil to create this composite cathode film. The atomic force micrograph of Figure 6 shows that the particle orientation includes particles with the basal or **c** axis oriented normal to the surface plane, as evidenced by the smooth, flat facets, combined with some degree of particle tilt resulting in the **a** axis (parallel to the graphene planes) intersection with the battery electrolyte. This composite film morphology results largely because of the shape of the particles (as platelets) and the processing method. As shown below, this morphology is well simulated by individual particles fixed onto planar electrode substrates.

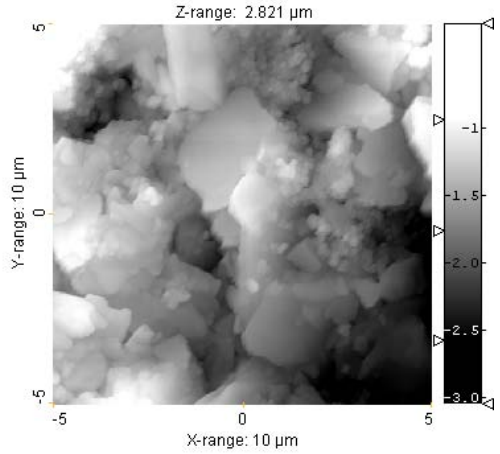

Figure 6. AFM image of a Sandia composite CF_x cathode.

Single particles can be fixed onto flat Au surfaces by modifying the Au with a short chain alkanethiol and relying on Vander Waals forces. Figure 7a shows an atomic force micrograph of two sub-micron sized particles in the upper portion of the image and a larger particle in the lower half of the image. The larger particle shows a good deal of morphology on the upright facing facets of the particle. Flat, planar regions appear to be oriented with their c-axis upright or normal to the Au surface. Regions of high step density exist between **c**-plane terraces where the **a**-axis is graphene edges are exposed. A particle fixed in this geometry still provides plenty of perimeter access for the release of F during cathodic discharge and an opportunity to track the formation of the graphite intercalation compound formation. Figure 7b shows a scanning

tunneling micrograph of a portion of a CF_x particle on a Au substrate. This image demonstrates that significant electronic conductivity exists within the particle and at the particle-Au interface to support tunnel-based imaging. Au terraces are clearly visible in the lower right hand corner of this image, while the highly stepped edge of the CF_x particle appear in the center to upper left of the image.

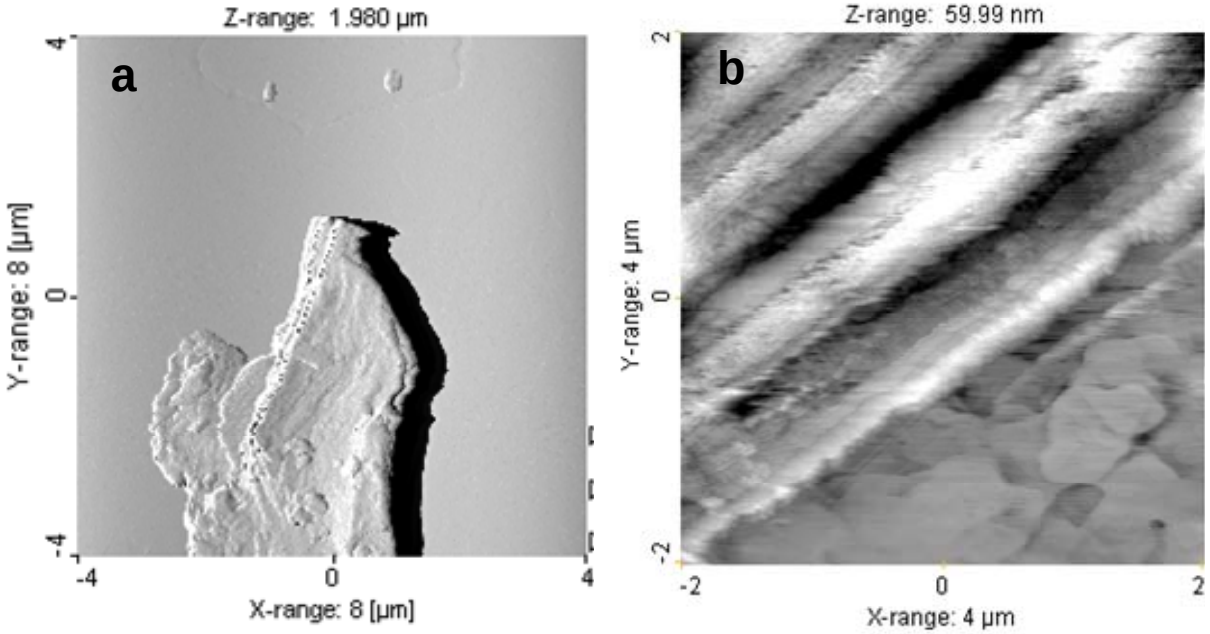

Figure 7. AFM (a) and STM (b) images of CF_x particles fixed on an Au surface.

Discrete laminae can be seen in the center of this image, which at this resolution are most likely ensembles of the terminus of graphene planes at this particle edge. These results clearly demonstrate that single particle can be fixed on planar electrodes and relevant details of the particle structure critical for the study of F egress and graphite intercalation compound (GIC) formation during cathodic discharge can be imaged and therefore studied. Continued work in FY06 will focus on demonstrating in situ imaging during the discharge process. A glove box for housing the SPM instrument under a controlled atmosphere has been designed and fabricated in order conduct these experiments. Single particles can also be characterized in order to determine local compositional changes. Figure 8 shows a TOF-SIMS secondary positive ion image set for a CF_x particle fixed on Au. Primary positive ions are C^+ (Fig. 8a) and CF^+ (Fig. 8b). These images are the result of cumulative ion generation between periods of sputtering and therefore represent the integrated composition through the outermost graphene layers. Individual layer images can be reconstructed as essentially a 3 dimensional map once the sputter rate has been quantified. Larger particles can be used for this purpose using AFM after the fact to measure sputter depth into the material. The variation in secondary ion yield with sputtering is shown in the formal sputter depth profile shown in Figure 9. Good signal-to-noise ratio exists for the relevant ion yields for the first series of graphene layers, before the limits of kinematic damage are reached in the particle bulk. This signal integrity will allow for sufficient 2 dimensional imaging at a given graphene layer to discriminate between fluorinated carbon at the particle center and an evolving de-fluorinated zone at the particle perimeter. A demonstration of this compositional characterization is a focus of our remaining FY06 activities.

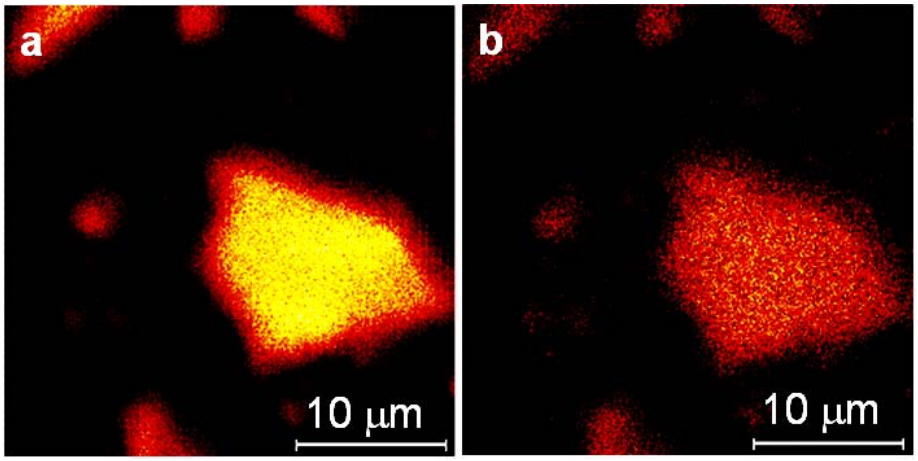

Figure 8. Positve secondary ion images of a CF_x particle fixed to an Au surface: a) C+ and b) CF+.

The depth profile of Figure 8 was acquired at the center of the particle.

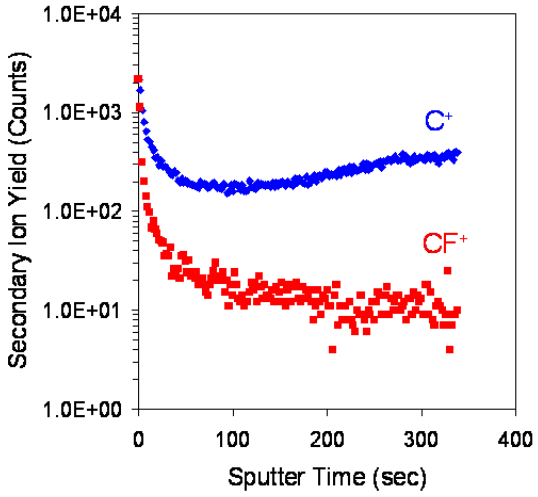

Figure 9. TOF-SIMS sputter depth profile of a single CF_x Particle fixed on a Au electrode.

2.2 FY'07-----2nd Year

In FY07 we investigated $(CF)_n$ materials from 3 different sources to further optimize cell performance for rate capability and temperature. We have successfully identified the presence of the intermediate by performing Multivariate Analysis on the X-ray data. A full paper has been published in the Journal of Applied Crystallography which has been copied below (Appendix B).

Additionally, we studied kinetics of de-fluorination and GIC formation in CF_x single particles using STM type techniques developed in FY06.

In this FY two new activities were initiated to perform F-NMR on CFx electrodes discharged to different depth-of-discharge (DOD) and Raman to monitor the local changes in the graphene planes while discharging cell. F-NMR work was performed in collaboration with City University of New York (CUNY) and the Raman work was performed with Lawrence Berkeley National Laboratory (LBNL).

The second segment describes the accomplishments of **TOF-NMR** (Time of Flight NMR), **STM** (Scanning Tunneling Microscopy), **AFM** (Atomic Force Microscopy**)** etc.

2.2.1 Accomplishments

Two full papers were published in the current FY. These are:

- "Performance Enhancement at Low Temperatures and In-situ X-ray Analyses of Discharge Reaction of Li/$(CF_x)_n$ cells" Ganesan Nagasubramanian, Mark Rodriguez, J. Power Sources (published)
- "In-situ XRD Analysis of $(CF_x)_n$ Batteries: Signal Extraction by Multivariate Analysis" Mark A. Rodriguez, Michael R. Keenan, and Ganesan Nagasubramanian – J. Applied Crystallography (published).

Prepared electrodes with optimum performance.

- For electrode optimization study, we investigated 4 different $(CF_x)_n$ materials purchased from different sources. The electrodes were made using Sandia in-house facility. We chose the best performer based on the electrochemical data obtained in coin cells.
- We prepared using, SNL in-house facility, three 18650* Li/$(CF_x)_n$ cells and adjusted them to different SOCs (State-of-Charge) for F-NMR and C-NMR studies at CUNY.
  *Cylindrical cell with 1.8 cm diameter and 6.5 cm high.
- We also prepared and conditioned several special* $(CF_x)_n$ electrodes for Raman studies by LBNL. The electrodes for the Raman study didn't contain any conductive carbon to eliminate scattering and obscuring of the signal from the partially discharged $(CF_x)_n$ electrode. We electrochemically discharged the cells to a predetermined SOC (State-of-Charge) and provided them to LBNL for Raman analyses. *These electrodes don't have additive carbon in

order to eliminate unwanted fluorescence background that would mask the useful Raman signal.

- We performed MVA (Multi-Variant Analysis) on the x-ray results (collected at Sandia) and showed for the 1st time the presence of an intermediate in the discharge reaction of the Li/$(CF_x)_n$ cell.
- Detected the initial stages of sheet exfoliation during carbon monofluoride reduction and ion:solvent intercalation using in situ AFM.
- Demonstrated successfully single carbon monofluoride particle imaging on inert electrode surface.

2.2.2 Electrochemical Testing of Cells in 2032* configuration

* Coin cell with 2 cm diameter and 3.2 mm thick

A typical discharge curve for one of the SNL-Built coin cell is shown in Figure 10. The open circuit voltage is around 3.4 V. The operating voltage is around 2.6 V even for a low discharge rate (C/100). We tested several cells to check for reproducibility. The coin cells performance is extremely reproducible and a paper has been published which is copied below (Appendix C).

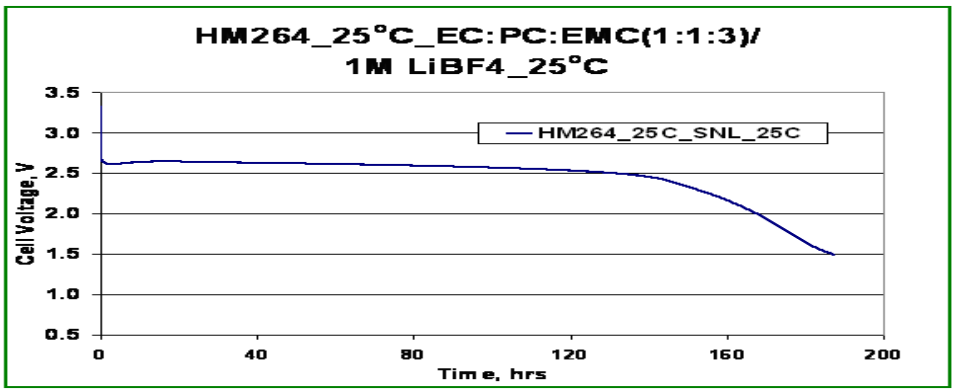

Figure 10. Discharge curve for an SNL built $(CF_x)_n$ coin cell at 25°C.

2.2.3 X-ray studies

A summary plot of both the voltage curve obtained during discharge of our pouch cell, along with a contour plot of the XRD data collected using a Siemens D500 θ–θ diffractometer (Cu Kα, λ = 1.5406 Å) are given and explained below.

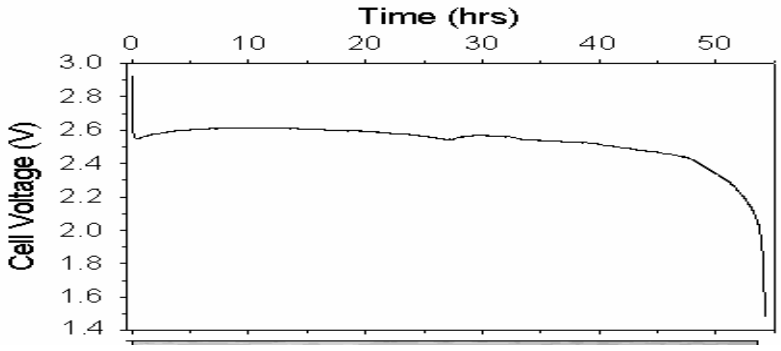

Figure 11. Discharge curve for our pouch cell.

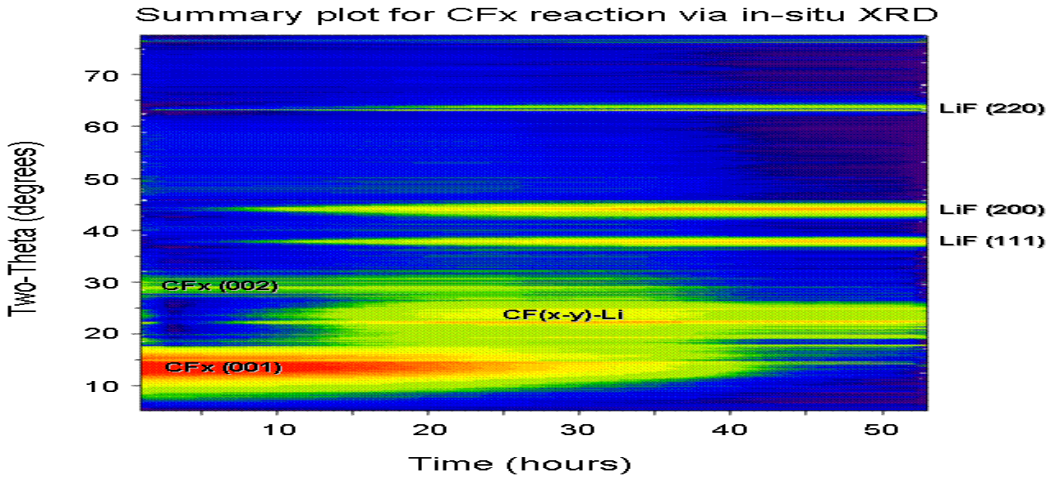

Figure 12. A contour plot of the XRD data collected during discharge.

The voltage curve shows typical discharge behavior for $(CF_x)_n$, with a precipitous drop from OCV at the onset of the discharge process, to a plateau voltage of ~2.6 V. This plateau voltage persists until the onset of cell failure. The XRD analysis is shown below the voltage curve as a contour plot, having axes of x = time, and y = 2θ angle and the intensity (as a log scale) shown as a color scale. The contour plot shows significant presence of the $(CF_x)_n$ cathode material at the beginning of cell discharge as illustrated by the prominent $(CF_x)_n$ (001) intensity at ~10° 2θ. The contour plot shows the $(CF_x)_n$ intensity dissipating as the cell progresses through discharge. LiF peaks are observed to mature concurrent with the decay of the $(CF_x)_n$ intensity. These observations are consistent with other published results[1]. A thorough analysis of the XRD data using multivariate analysis (MVA) cleanly separated the $(CF_x)_n$ feature from scattered intensity due to the fixed components of the pouch cell (e.g. separator). Moreover, the MVA technique suggested that another species, perhaps an intermediate phase, formed during cell discharge as well shown in the contour map as $CF_{(x-y)}$ -Li. An in-depth discussion regarding these

observations, along with further detail regarding MVA of the obtained XRD dataset has been published in the Journal Applied Crystallography for publication.

2.2.4 F-NMR Results (Professor Steve Greenbaum; CUNY)

We made three 18650 cells and discharged them to different SOCs (State-of-charge). We supplied CUNY the cells for F-NMR studies on the $(CF_x)_n$ cathodes.

Sample Preparation for NMR Studies

The three 18650 cells provided by Sandia National Laboratories discharged to different SOCs (State-of-Charge) were cut open inside an argon-filled, controlled atmosphere glove box for extracting the cathode material and the samples were packed into airtight 4mm and 1.7mm rotors in the box for NMR studies. In addition, the un-cycled starting material was dried overnight at 100 ^{o}C in a vacuum oven before packing. The ^{19}F Nuclear Magnetic Resonance (NMR) data was collected using a Varian NMR 500MHz magnet, externally referenced to $CFCl_3$, using Magic Angle Spinning (MAS) and a spin-echo pulse sequence, techniques employed to reduce the homo- and hetero- dipole interactions experienced by the fluorine nuclei. Figure 13 shows the ^{19}F NMR spectra overlapping corresponding to the expected compounds present: a prominent PVdF signal (near –15ppm), present in all samples including the starting material; a strong LiF signal (near 130ppm), seen only in the cycled samples; a narrow (suggesting mobility) $LiBF_4$ signal (84ppm); and a small shoulder (near –150ppm), characteristic of intercalated fluorine. This latter signal is more prominent in the 80% versus the 50% discharged sample.

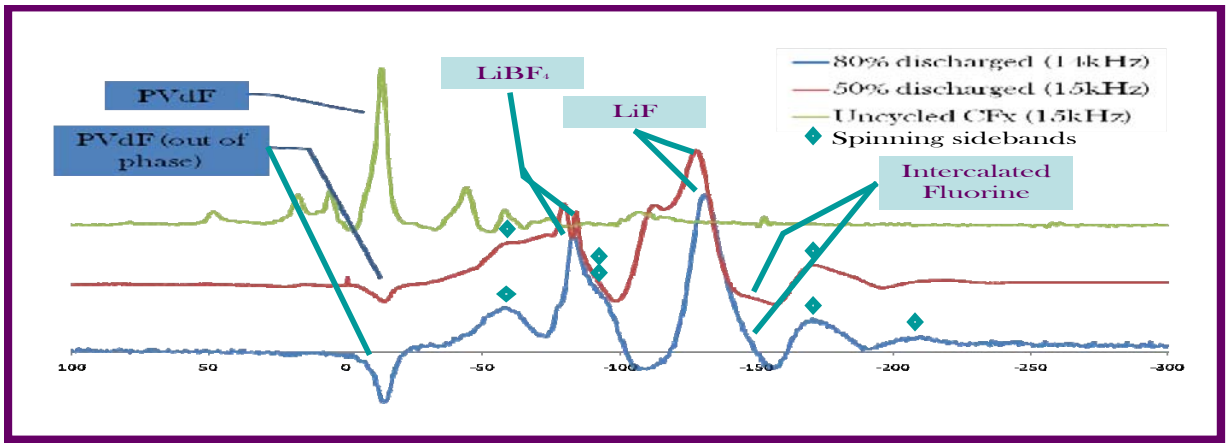

Figure 13. 19F MAS NMR of $(CF_x)_n$ cathodes cycled against lithium to different voltages.

2.2.5 Raman Studies

LBNL is equipped with tools to probe the battery electrode structure in-situ and ex-situ. I took advantage of this unique capability and worked with Robert Kostecki to probe $(CF_x)_n$ cathode electrode using Raman. Sandia provided LBNL with specially made and conditioned $(CF_x)_n$ electrodes for performing ex-situ Raman studies. In addition, we provided them with $(CF_x)_n$

powder and its precursor (graphite carbon) for control measurement. Figures 14 and 15 show ex-situ Raman spectra collected on Sandia supplied graphite precursor and the partially discharged electrode. Raman spectra of $(CF_x)_n$ powder and electrode (undischarged) are not shown here since no discernable peaks were observed- mostly fluorescence was observed.

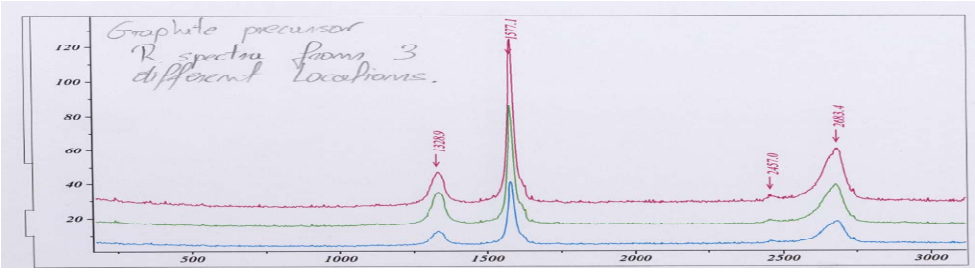

Figure 14. Raman spectra of precursor graphite carbon.

Figure 14 shows three spectra collected at three different spots of the graphite powder particle. The response is typical Raman response of graphene structure. The intensity plotted on the y-axis is not very high which suggests that this material doesn't fluoresce. Figure 10 shows Raman spectra for the partially discharged electrodes (black and red) and for the fresh electrode (not discharged; green). For the partially discharged electrodes in addition to the two peaks at 1328 cm^{-1} and 1577 cm^{-1} (see Figure 10) there is an additional peak at around 1600 cm^{-1}. This extra peak, we believe, is coming from the local changes in the graphene plane due to discharge. This observation gives us some measure of confidence that it is possible to see changes in the graphene planes by Raman technique. The spectrum for the fresh electrode (green) shows only fluorescence as expected.

The collaborative studies with CUNY and LBL were not continued into FY08 and so no work on F-NMR and Raman was performed in FY08

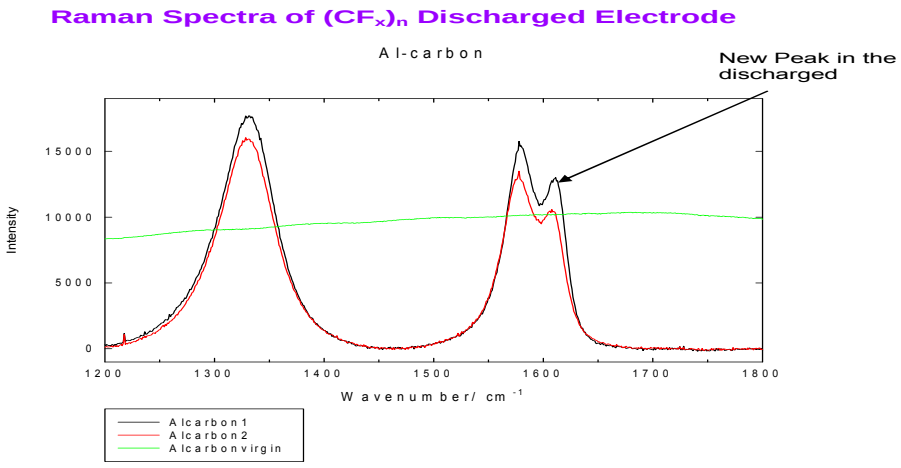

Figure 15. Raman spectra of partially discharged electrodes.

2.2.6 STM Type Studies

Detected the initial stages of sheet exfoliation during carbon monofluoride reduction and ion:solvent intercalation.

Figure 16 shows a series of *in situ* AFM images for a $(CF_x)_n$ film (10% Polyvinylidene difluoride binder and graphite) at several stages of cathodic charging. Intercalation was conducted in a 1 M $LiBF_4$:propylene carbonate electrolyte using a constant current. The images were generated in an attractive intermittent contact mode using a magnetically coated lever and an AC magnetic field to drive the cantilever at a 10 kHz frequency. The ridge that runs down the approximate center of the 3-D image in Figure16a represents the exposed edge plane (a aixs) of single carbon monofluoride particle. Assuming a 0.58 nm interlayer spacing between carbon sheets with fluorine interspaced, the measured ridge height of ca. 230 nm corresponds to the exposure of 400 carbon fluoride sheets. No changes in this structure were observed for an initial 20 milliCoulomb (mC) polarization when compared to the initial local topography after several hours of equilibration at open circuit. Figure 16b shows the local topology after an additional 60 mC has been passed. Some drift (image compression along the y-axis, a drift to the left along the x-axis) is evident, but no change is detected in the height of this carbon monofluoride sheet stack and no changes are evident in the surface texture of the basal plane of this particle. Figure 16c shows that topographic changes start to take place at 120 mC cumulative charge. The ridge height above the adjacent grain has increased to 520 nm indicating that the monofluoride has undergone reduction and vertical expansion with the formation of a graphite intercalated compound (GIC). Vertical height increases due to Li cation insertion, association with fluoride anion, and possibly solvent intercalation into the crystal edge. This height change of an approximate factor of 2.3 is considerably greater than an expected ratio of 1.6, based on 0.94 nm for a Li intercalated carbon monofluoride and 0.58 nm for the starting material. This difference could reflect the inclusion of propylene carbonate into the GIC, as this solvent has been proposed to participate in Li insertion chemistry for pure graphite.

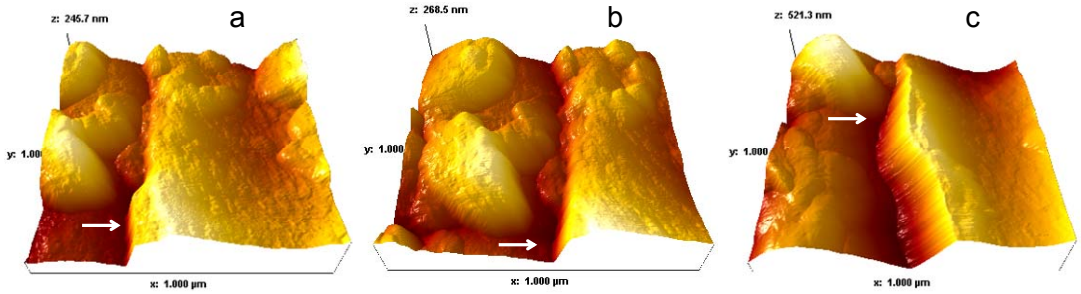

Figure 16. Topographic AFM images after cathodic polarization of a carbon monofluoride electrode in 1 M $LiBF_4$ propylene carbonate.

Arrows indicate the approximate point of comparison along a monofluoride edge plane – the site for GIC formation. The vertical difference measured indicates reduction and GIC formation is taking place.

What is learned from this type of experiment is that the intercalation process can occur at a fairly early stage during cathodic discharge of the monofluoride. No evidence of film formation from solvent breakdown or intercalation into partial monofluoride sheets, presumed to create the basal

plane surface texture, occurs. The process being observed is a relatively low activation energy process for the monofluoride reduction in an energetically heterogeneous material. These results show that early stages of GIC formation can be tracked using in situ AFM. These early stage processes are viewed as the critical chemistry responsible for the undesirable cell voltage reduction in primary batteries based on the Li: $(CF_x)_n$ electrode pair.

- Successfully demonstrated single $(CF_x)_n$ particle imaging on inert electrode surface

The idea is to locate individual carbon monofluoride particles on electrodes that serve as current collectors. Cathodic polarization is used to intercalate the particle to some extent. The particle can then be analyzed using combinations of time-of-flight secondary ion mass spectrometry (SIMS) and transmission electron microscopy (TEM). The use of a alkyl thiol (decane thiol) is used to attract carbon monofluoride particles on a gold electrode. Specific size range particles are retained on the electrode surface with electrolyte introduction and AFM imaging. The intent is to conduct intercalation with imaging and then conduct ex situ compositional and structural analysis of the intercalated particles.

Again this work also was not carried on into FY 08 and so no more work was performed in FY08.

2.2.7 Summary of Accomplishments

- Performed MVA analysis on the in-situ x-ray data and identified unequivocally the presence of an intermediate. To my knowledge we are the first to confirm the presence of an intermediate.
- Two full papers and one proceedings paper were written. One of the full papers has been accepted for publication in the J. of Power Sources and the other has been submitted to the J. Applied Crystallography.
- Provided CUNY with three 18650 cells for F-NMR, C-NMR studies and the data is being analyzed in depth. Initial results indicate that these techniques are suitable for monitoring changes caused by the discharge reaction in the graphene planes of the cathode.
- Prepared special electrodes for ex-situ Raman studies. The initial results show that Raman technique can be advantageously used to monitor changes in the graphene structure.
- Detected the initial stages of sheet exfoliation during carbon monofluoride reduction and ion:solvent intercalation.
- Demonstrated successfully single carbon monofluoride particle imaging on inert electrode surface.
- Investigate the intermediate reactions occurring in the $(CF_x)_n$ material in the presence of lithium, by molecular dynamics simulations. The General Reactive Atomistic Simulation Program (GRASP) developed at Sandia will be used with a reactive forcefield (ReaxFF developed at Caltech). These simulations will provide atomistic detail about the reactions that occur including the products, reactants, and intermediate compounds. Simulation is able to observe small changes in stoichiometry and chemical bonds. Therefore, information can be obtained that is difficult to acquire experimentally that

complements the X-ray diffraction data and makes a more complete picture of the physical processes during cell discharge.

- Conduct If the above activities are successful and complete then we will issue a contract to a $(CF_x)_n$ manufacturer to produce $(CF_x)_n$ powder with improved voltage performance.

2.3 Accomplishments for FY 08

2.3.1 Two different modeling efforts were funded in this FY

The first model involves the molecular dynamics simulation of Li/$(CF_x)_n$ discharge reaction This work was performed at Sandia National Labs in Org1814. The other model, Density Functional Theory, was performed by Professor Chris Wolverton at Northwestern University, Chicago. Both these models suggest the presence of an intermediate in the discharge reaction which is in concurrence with what I have shown experimentally. The accomplishments of the two modeling works are given below.

2.3.1.1 Molecular Dynamics Simulations of Lithium Ions in $(CF)_n$

2.3.1.1.1 Introduction

Molecular dynamics simulations are often used to provide insight into the behavior of materials at the atomic level. The purpose of this work was to attempt to provide insight into the unexpected behavior of lithium batteries that are based on fluorinated graphite $(CF_x)_n$. Experimentally, the voltage drop across these batteries is observed to be much less than expected from thermodynamic calculations of the assumed reactions. Thus, it would be very handy to be able to watch what occurs in this system at an atomistic level.

The greatest difficulty in performing any simulation is simplifying the physical situation to make the calculations tractable, yet still capture the relevant behavior. The concern is that by simplifying the problem, spurious behavior may result or unphysical results obtained. In an effort to prevent such difficulties, simulation model systems are usually built in stages. That is the case here. While ideally one could start with atoms jumbled together in a box and watch them assemble into the desired material, practically, systems are carefully constructed to have the structure and topology determined from experiments. Complicated systems are built in stages so that intermediate behaviors can be checked and modifications made to ensure that the testable simulation results accord with experiment, lending more confidence that predictions from simulation are useful.

This work used followed the idea of constructing simple systems and then adding complexity in steps to get to the desired simulation. The plan was to use fixed topology classical molecular dynamics simulations on increasingly complex systems and then switch to reactive force field simulations[1,2.] to get the detailed reactions in the complex system. Unfortunately, the preliminary work with the fixed topology systems showed that small defects in the system, defects guaranteed to be present in varying and un-quantified levels in the experimental samples, make using the reactive force field unreliable because the resulting behavior will be too dependent on the given initial state of the system. This is doubly true because the reactive force field parameters were already in the process of being updated this spring to reduce recently

discovered inaccuracies for similar systems. Thus, no simulations with reactive force fields were performed in this work and all results shown are from classical fixed topology simulations.

2.3.1.1.2 Theory and Methods

In the simplest terms, molecular dynamics simulation is the integration of Newton's equations of motion for a system of atoms[3]:

$$\vec{F} = m\vec{a} \tag{1}$$

The force is determined from the derivative of the potential energy interactions of the atoms. Choosing the integration method and potential energy interactions for a specific system is an art. For this work, the Large-scale Atomic/Molecular Massively Parallel Simulator (LAMMPS) program[4] developed at Sandia was used. This program was chosen because it is a widely used program that has a track record of giving good results, provided that proper input is supplied.

To calculate the forces on each atom, classical molecular dynamics relies on a system of potential energy equations based on the different types of interactions. For this work, the relevant types of interactions are bonds, angles, torsions, Coulombic interactions, and excluded volume. The parameters for the atoms in the simulation came from the universal force field[5]. The non-bonded interactions were truncated at 10 Å. A neighbor list was constructed with a binning procedure and the skin radius was 2.0 Å. 1-2 and 1-3 interactions were not included in the non-bonded interactions.

Of course, Newton's equations of motion are only valid for a constant energy calculation. To better approximate experimental conditions, a thermostat and a barostat are often applied to control the temperature and the pressure of the simulations. For the simulations performed here, a Nose-Hoover thermostat was applied with a time constant of 1.0 fs. When the barostat was applied, it was also of the Nose-Hoover type and had a time constant of 10 fs. A time step of 0.1 fs was used.

The largest system used in this study started as 512 carbon atoms arranged in four layers of graphite. To emulate a bigger system, the standard practice of applying periodic boundary conditions was employed. Periodic boundary conditions were applied in all three directions with care taken so that the graphite sheets would be continuous across the box, thus necessitating the small time step used.

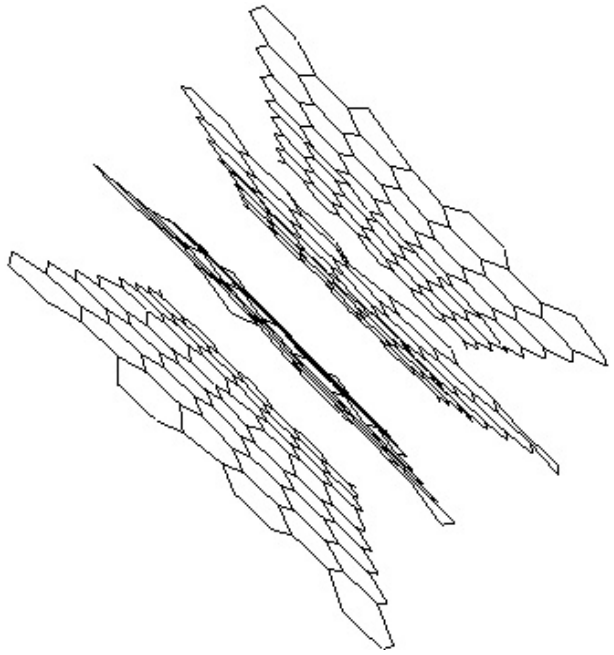

Figure 17. Initial Graphite System.

The spacing between adjacent layers of the graphite matched the experimental value of 3.35Å. This point is important because adding the fluorine to the graphite system expands the interlayer distance. This expansion is a result not just of adding the relatively large fluorine atoms into the gap, but is exacerbated by the resulting deformation of the carbon bonding from a planar geometry to a tetrahedral geometry. Experiment has shown[6] that the resulting interlayer distance is usually between 5.8 and 8.9Å.

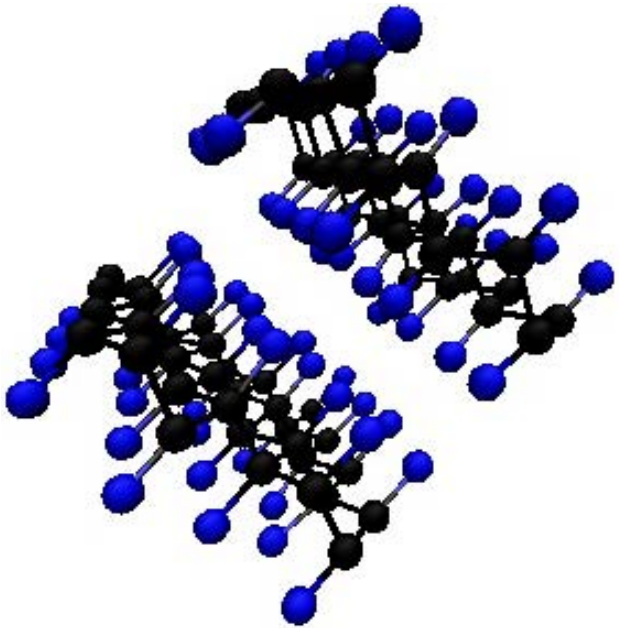

Figure 18. Fluorinated Graphite: $(CF)_n$.

The exact value of the interlayer spacing depends on a few factors. According to the literature, experiments show that one of the primary factors is the extent of fluorination. A F/C ratio of 0.94 was observed to have a gap of 6.00 Å, while a F/C ratio of 0.93 gave a spacing of 5.84Å. One reason for this variation, which is a complicating factor for simulation, is that the type of bonds between fluorine and carbon in these systems vary from ionic to covalent due to degree of fluorination[7]. Thus, the actual size of the fluorine and the charge on it will be different depending on how many other fluorine atoms are present in the immediate vicinity. These variations introduce an additional complexity for simulation because, while number of fluorine are fixed at the beginning of the simulation, checking for possibilities of reactions with lithium will be heavily dependent on charge and size of the fluorine. For all the systems here, the F/C ratio was exactly one. However, to investigate the effect of varying nature of the fluorine-carbon bond, simulations were performed with charges in both the covalent and ionic limits.

2.3.1.1.3 Results and Discussion

Adding lithium to the prepared systems lead to some interesting observations. A single lithium ion in the system with the covalent level of charge (-0.1 on the fluorine atoms) shows a pronounced bending of the layers next to the lithium ion. Changing the charge on the fluorine atoms to be the ionic value of -1 lead to an unstable system in which the layers flew apart.

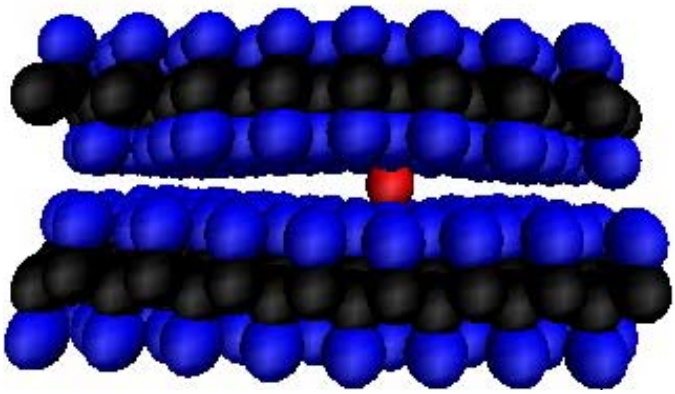

Figure 19. System with one Li^+ and a fluorine charge of -0.1.

Varying the loading of the lithium also had an effect on the structure of the layers. As one might expect, having two lithium ions near each other on opposite sides of a layer means no bending in their vicinity. Otherwise, bending still occurred by the atoms near the lithium. No clustering of the lithium ions was observed and lithium ions in different layers appeared to have minimal effects on each other.

In all cases, the lithium ions were observed to be mobile with a jumping motion between evidently preferred locations. With systems of this size, measuring diffusion coefficients are meaningless because of the spurious effects due to each layer being a continuous two-dimensional surface. Physical systems will have defects so that the lithium ions can jump between layers and move along grain boundaries. Including those defects in these simulations

would lead to either systems that are too large for current computing capabilities or systems that have too high a concentration of those defects. Edge effects will be noticeable in physical systems, but including them here by turning off the periodic boundary conditions would lead to a huge overemphasis on them.

2.3.1.1.4 Conclusion

Molecular dynamics simulations were performed on $(CF)_n$ systems with fixed topology. These systems were simplified models of the physical systems that were chosen to be computationally tractable. It was determined that defects in the physical model probably account for most of the reaction sites. Seeding the simulations with those defects was not feasible. Too much would depend on initial configurations with abnormally high levels of those defects due to the small system sizes. Simulating larger system sizes with the fixed topology is feasible, but using systems large enough to have a physical concentration of defects is not a feasible option when using the reactive force fields.

2.3.1.1.5 References

1. A.C.T. van Duin, S. Dasgupta, F. Lorant, and W.A. Goddard, III "ReaxFF: A Reactive Force Field for Hydrocarbons" J. Phys. Chem. A, 105, 9396 (2001).
2. S.S. Han, A.C.T. van Duin, W.A. Goddard III, and H.M. Lee "Optimization and Application of Lithium Parameters for the Reactive Force Field, ReaxFF" J. Phys. Chem. A 109, 4575 (2005).
3. M.P. Allen and D.J. Tildesley *Computer Simulations of Liquids* Oxford University Press: Oxford (1987).
4. S. J. Plimpton "Fast Parallel Algorithms for Short-Range Molecular Dynamics" J. Comp. Phys. 117, 1 (1995). Program available from http://lammps.sandia.gov/
5. A.K. Rappe, C.J. Casewit, K.S. Colwell, W.A. Goddard III, and W.M. Skiff "UFF, A Full Periodic Table Force Field for Molecular Mechanics and Molecular Dynamics Simulations" J. Am. Chem. Soc. 114, 10024 (1992).
6. N. Watanabe, S. Koyama, H. Imoto "Thermal Decomposition of Graphite Fluoride. I. Decomposition Products of Graphite Fluoride, $(CF)_n$ in a Vacuum" Bull. Chem. Soc. Jpn., 53, 2731 (1980).
7. S.L. di Vittorio, M.S. Dresselhaus, G. Dresselhaus "A model for disorder in fluorine-intercalated graphite" J. Mater. Res. 8, 1578 (1993).

2.3.1.2 Identifying intermediate in the discharge reaction of the Li/(CF*x*)*n* cell and understanding effect on cell voltage

2.3.1.2.1 Abstract

Professor Wolverton and Dr. Shin of Northwestern University have used first-principles calculations based on density functional theory (DFT) to derive the open circuit voltage profiles of Li/$(CF_x)_n$ cells. They wish to understand and explain the significant difference between the thermodynamic calculation of the cell voltage (~4.5 V) and the observed operating cell voltage (3.2 V). One theory suggested in the literature to explain this voltage reduction involves the formation of a ternary compound in the reaction sequence which governs/controls the open circuit voltage (OCV): For the discharge reaction, $x\text{Li} + (CF_x) \rightarrow C + x\text{LiF}$, the OCV should be ~4.5 V from available, well-established thermodynamic data (essentially, the difference in heats

of formation of LiF and CF_x) . However, the observed OCV is around 3.2 V. In our project, we have used DFT calculations to study the thermodynamics of the above reaction, and also the possibility of a stable ternary intermediate phase. They also analyze the thermodynamics of the reaction, and assert that a stable ternary intermediate cannot reconcile the discrepancy between observed and thermodynamic calculations of the voltage. The discrepancy could only be explained via a non-equilibrium ternary intermediate pathway. They also find that DFT is not well suited for an accurate description of the CF_x-type systems, presumably due to well-known deficiencies of DFT for treating van der Waals bonding, and molecular systems in general. They have attempted to use quantum-chemical cluster-based methods in an attempt to rectify the DFT results, without success. In an attempt to ascertain whether DFT can be accurate for other Li electrode reactions (e.g., not involving van der Waals bonding or molecular systems), they have performed studies of a recently proposed Li-ion anode material ($LaSn_3$), and find that the DFT predictions are excellent. Thus, extensions of DFT, high order quantum chemical methods, or quantum Monte Carlo based methods will presumably have to be used to study the CF_x reactions.

2.3.1.2.2 Introduction

The open circuit voltage (OCV) of the discharge reaction for the Li/$(CF_x)_n$ cell may be simply calculated from available thermodynamic data for the heats of formation of LiF and CFx. Such a calculation yields ~4.5 V for the OCV. However, the observed OCV is around 3.2 V. This difference (~ 1.3 V) in voltage between the theoretical and the measured is quite significant as it reduces the delivered energy from a potential value of 3900 to 2200 Wh/kg. So there has been a strong desire in the community to understand (and perhaps mitigate) this decreased voltage. One possible theory which has been asserted in the literature [1, 2] to explain this voltage reduction involves the formation of a ternary compound in the reaction sequence which governs/controls the OCV.

Figure 20 shows a schematic of the energetics of the CF_x/LiF reaction. The OCV is related to the chemical potential difference of Li in the cathode vs. anode, and in the plot of the energy vs. composition, the average voltage of the reaction (the voltage integrated over composition) can be easily shown to be related to the slopes of the lines connecting various points. Thus, the slope of the line connecting CF and LiF is labeled ~4.5V, for instance. This plot then offers a convenient graphical method to assess the possibility of a ternary intermediate: Clearly, if a ternary intermediate is the explanation for the observed 3.2V OCV, then it must lie *above* the line connecting CF and LiF. Of course, this means that the ternary intermediate is unstable with respect to decomposition into CF+LiF. On the other hand, a stable ternary intermediate would necessarily have to lie below the tie-line connecting CF+LiF, and hence would have an OCV greater than 4.5V. This discussion is all simply consistent with the well-known fact that during discharge, the voltage of a system decreases with increasing discharge. In other words, if there are multiple stable phases in a system, discharge into the initial phase always is at the highest voltage, and subsequent discharge is at lower voltages. In the system of Fig. 20, this simply means that the initial ternary intermediate, if stable, would give a voltage higher than the CF/LiF reaction, and subsequent steps would result in a lower voltage. In sum, then, the simple schematic of Fig. 20 illustrates the important point that *a stable ternary intermediate cannot explain the discrepancy between thermodynamic calculation and observed OCV of the CF_x/LiF system.*

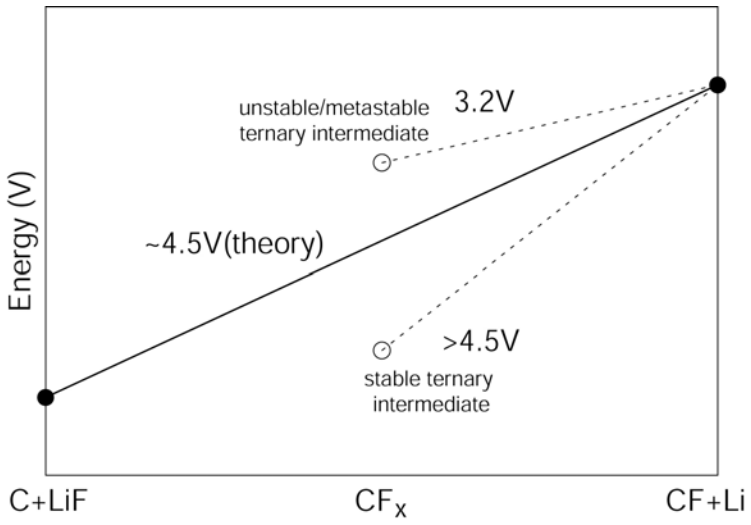

Figure 20. Schematic diagram of voltage change for Li/$(CF_x)_n$ cell discharge reaction.

2.3.1.2.3 First-principles calculations

Here, we use first-principles density functional theory (DFT) calculations in an effort to help accelerate the search for novel battery reactions. Quantities directly relating voltage and structural stability may be computed from DFT, and thus these computations can be used as a "screen" for predicting improved materials. Wolverton *etal* have calculated total energies of individual phases from first-principles in the discharge reaction to predict the OCV. It has been shown by a large number of researchers that first-principles calculations DFT calculations accurately predict the properties of a wide range of solid state materials. However, there are also well-known failures of DFT: Mott insulators and highly correlated systems, some magnetic materials, van der Waals bonded/molecular solids, etc. And, current implementations of DFT are also known to be much less quantitatively accurate for molecules than they are for solids.

They use the Vienna Ab initio Simulation Package (VASP)[3, 4] to perform the electronic structure calculations. The projector augmented wave (PAW) method[5] was selected and the generalized gradient approximation (GGA)[6] was used for exchange and correlation contributions to the Hamiltonian of the ion-electron system. Energy cutoff was set as 875 eV for all the calculations and an isotropic mesh of 5000 *k*-points per primitive cell was used based on Monkhorst-Pack scheme[7].

2.3.1.2.4 Cluster calculations

As an alternative tool to calculate total energies of each phase that participate the discharge reaction of Li/$(CF_x)_n$ cell we have used GAMESS (General Atomic and Molecular Electronic Structure System) [8, 9] in the present work. For wavefunctions, a high spin open shell SCF (ROHF) has been used as implemented in GAMESS.

2.3.1.2.5 Results and discussions

In order to compute the OCV of discharge reaction, we begin by computing the VASP energies of the individual phases in the xLi + (CF_x) $\rightarrow$ C + xLiF reactions. Calculated total energies for

the phases other than CF_x are shown in**Error! Reference source not found.**. It should be noted here that we have used total energy of diamond carbon in the OCV calculation instead that of graphite. Graphite is a layered structure with van der Waals interaction between layers (absent from DFT), and hence we suspect that total energy calculation of graphite would not be nearly as reliable as that of diamond. However, the energy difference between the diamond and graphite phases for carbon is known to be very small so that this use of the diamond structure will not make any significant difference in OCV calculations.

Table 1. Calculated total energies for C, Li, and LiF from first-principles calculations.

Structures	Prototype	Total Energy (eV/f.u.)
C	Diamond	-6.2614
Li	W	-1.8999
LiF	CsCl	-9.6941

First, we have considered the discharge reaction, when x=1 (i.e., CF), then the reaction can be rewritten as:

$$Li + CF \rightarrow C + LiF \quad (1)$$

So, the remaining phase to compute from DFT is CF. However, it should be noted that they anticipate that this polymeric material might be problematic within DFT, so they explored previous literature on the topic. In 1993, Charliere *et al.*[10] have studied structural and electronic properties of carbon monofluoride (CF) from first-principles. They have studied two different conformations, which are denoted as boat and chair, respectively. Wolverton *etal* wish to reproduce their reported crystalline parameter for both phases. Calculated total energies and corresponding OCVs are shown in**Error! Reference source not found.**.

Table 2. Calculated OCV for boat and chair phases from Charlier *et al*.[10].

Designation	Total Energy (eV/atom)	Calculated OCV (V)
Boat	-6.2787	1.5
Chair	-5.2405	3.6

Interestingly, according to Charliere *et al*.[10] (who used the local density approximation in their calculations) the chair CF conformation has a lower than boat, however, we find the opposite (using the generalized gradient approximation). And, for our lowest-energy conformation (boat), we find a calculated OCV that is much lower (1.5V) than observed.

Because we suspected that the polymeric structure of CF might pose difficulties for the DFT-GGA, we decided to try searching for another low-energy structure of CF that we might use in the voltage calculations. The motivation behind this search was not to propose a novel crystal structure for this phase, but rather to find a dense, non-polymeric form of CF that DFT might predict as a ground state, which presumably would then have an energy close to the true polymeric ground state. The idea, then, is that this might serve as a reasonable energy to use for

CF in voltage calculations. The calculated energies of CF in about 30 possible "AB" structure types are given in**Error! Reference source not found.**, along with the calculated OCV for each structure. We find that the B29 (SnS-type) structure has the lowest energy and the corresponding OCV is 1.4V. Interestingly, this energy is quite close to the polymeric boat conformation for CF.

Table 3. Calculated OCVs for various CF structures. B29 has the lowest formation energy indicating amongst the most stable structure and predicted OCV is 1.4V.

Designation	Prototype	Total Energy (eV/atom)	Calculated OCV (V)
Ba	CoU	-5.4157	3.2
Be	CdSb	-5.4946	3.1
Bg	MoB	-5.5235	3.5
Bh	Wc	-3.3125	7.4
Bi	AsTi	-3.3123	7.4
Bk	BN	-3.1128	7.8
B1	NaCl	-3.0971	7.9
B2	CsCl	-3.0052	8.0
B3	Zincblende	-3.0185	8.0
B4	Wurtzite	-3.1248	7.8
$B8_1$	NiAs	-4.8777	4.3
B9	Cinnabar	-5.0821	3.9
B10	PbS	-3.5718	6.9
B11	γ-CuTi	-5.4701	3.1
B12	BN	-4.6803	4.7
B13	NiS	-5.4956	3.1
B16	GeS	-5.4935	3.1
B17	PtS	-3.5235	7.0
B18	CuS	-3.2041	7.6
B19	AuCd	-5.1924	3.7
B20	FeSi	-4.3946	5.3
B24	TlF	-3.0969	7.9
B26	CuO	-3.5233	7.0
B27	FeB	-5.3237	3.4
B29	SnS	-6.3248	1.4
B31	MnP	-5.1451	3.8
B32	NaTl	-3.1571	7.7
B34	PdS	-5.8960	2.3
B35	CoSn	-3.2157	7.6
B37	SeTl	-5.2116	3.6

Wolverton *etal* also have performed a similar crystal structure search for the energetics of the C_2F compound. The calculated energies and OCV for various structures are shown in**Error! Reference source not found.**. As shown in **Error! Reference source not found.** for CF calculations, the predicted OCV for the discharge reaction

$$Li + C_2F \rightarrow 2C + LiF \quad (2)$$

is quite scattered. The C23 ($PbCl_2$-type) structure has the lowest energy and hence is the most stable structure. In this case, the extreme stability of this C2F compound even leads to a negative OCV. Hence, we find that standard plane-wave DFT (within the GGA) is not suitably accurate to yield quantitatively accurate predictions for CF_x/LiF reactions.

Table 4. Calculated OCVs for various C_2F structures. C23 has the lowest formation energy indicating amongst the most stable structure. However its calculated OCV is negative.

Designation	Prototype	Total Energy (eV/atom)	Calculated OCV (V)
Ca	Mg_2N	-5.1595	4.8
Ce	$PdSn_2$	-6.1271	1.9
Ch	Cu_2Te	-6.6656	0.3
C1	Fluorite	-2.9562	11.4
C1b	MgAsAs	-2.9562	11.4
C2	Pyrite	-4.1104	8.0
C3	Cuprite	-3.1631	10.8
C4	Rutile	-5.1004	5.0
C5	Anatase	-4.7642	6.0
C6	Trigonal ω phase	-6.9190	0.5
C7	MoS_2	-6.7292	0.1
C8	High Quartz, SiO_2	-6.6368	0.4
C9	Ideal β-Cristobalite	-2.7030	12.2
C10	β-Tridymite, SiO_2	-3.3924	10.1
C11b	$MoSi_2$	-5.2347	4.6
C14	Laves ($MgZn_2$)	-4.6343	6.4
C15	Laves (Cu_2Mg)	-3.9187	8.6
C15b	$MgSnCu_4$	-3.9186	8.6
C16	Al_2Cu	-4.5236	6.7
C18	Marcasite	-6.0556	2.2
C19	α-Sm	-6.7494	0.1
C21	Brookite	-6.0364	2.2
C22	Fe_2P	-6.0890	2.0
C23	$PbCl_2$	-7.2214	-1.3
C24	$HgBr_2$	-6.6797	0.3
C32	Hexagonal ω	-6.5068	0.8
C34	$AuTe_2$	-6.7492	0.1
C35	$CaCl_2$	-6.1249	1.9
C36	Laves ($MgNi_2$)	-5.2655	4.5
C38	Cu_2Sb	-5.3715	4.2
C40	$CrSi_2$	-5.1612	4.8
C42	S_2Si	-6.1079	2.0
C43	Baddeleyite, ZrO_2	-6.5790	0.6
C46	Krennerite, $AuTe_2$	-6.6324	0.4
C49	$ZrSi_2$	-6.6743	0.3
C54	$TiSi_2$	-6.6789	0.3

Due to the difficulties with planewave DFT for this system, Wolverton *etal*. have also used the cluster-based quantum-chemistry tool, GAMESS, to calculate total energies of each phase that participating in the discharge reaction of $Li/(CF_x)_n$ cell. Unfortunately, Wolverton *etal* also found that GAMESS was insufficient to quantitatively predict the OCV reaction energy, presumably due to the difficulties in treating periodic systems and metals within GAMESS.

Since Wolverton *etal* found difficulties with DFT and quantum-chemistry-based methods for the CFx/LiF system, we wish to understand whether these difficulties are pervasive for Li "displacement" reactions, or whether they are specific to this system. Therefore, Wolverton *etal*

applied our planewave DFT methods to another recently-proposed displacement-type Li insertion material, $LaSn_3$. (This work was performed in collaboration with experimental work from J. Vaughey and M. Thackeray at Argonne National Laboratory, and a manuscript is in preparation.)

2.3.1.2.6 First-principles calculations of $LaSn_3$ as a Li battery anode

Wolverton *etal* report the results of our preliminary investigation of $LaSn_3$ as anode materials for lithium-ion batteries. $LaSn_3$ is an interesting candidate anode material due to the possibility of either displacement- or insertion-type reactions with Li.

Displacement Reactions: If $LaSn_3$ reacts with Li via displacement of La and formation of Li-Sn compounds, it potentially could exhibit a high theoretical specific capacity due to its high tin content. Specifically, a theoretical specific capacity of 650 mAh/g would be achieved based on a complete displacement of La via the reaction of 12 lithium atoms per formula unit (i.e., 4 Li per Sn atom):

$$12\ Li + LaSn_3 \rightarrow La + 3\ Li_4Sn$$

and a volumetric capacity of 4920 mAh/ml based on the density of $LaSn_3$ (7.57 g/ml). In practice, however, the volumetric capacity will be slightly lower because the electrode expands overall on lithiation. And, since other compounds with lower Sn content exist in the La-Sn phase diagram (e.g., La_3Sn_5), it is possible that La would only be partially displaced by Li, which would also result in lower capacity numbers. For simplicity and convenience in some of our general discussions, we assumed a maximum uptake of 4.0 Li per Sn atom.

Insertion-type Reactions: $LaSn_3$ has the prototypic Au_3Cu structure (cubic Pm-3m symmetry) which may be viewed from two different perspectives. One could think of this as a substitutional arrangement of La and Sn on an fcc lattice, and hence as a close-packed intermetallic compound with possible interstitial sites available for Li incorporation. Alternatively, one can view this structure as a "defect perovskite" with a vacant cation site. This vacant octahedral site at the body-centered position gives an interstitial space that might allow the incorporation of at least one lithium atom per $LaSn_3$ formula unit. In this hypothetical perovskite $LiLaSn_3$ structure, the Li atoms would be bonded predominantly to six nearest-neighbor Sn atoms. In order to understand more completely the reaction mechanism of $LaSn_3$ with Li, we report here on a coupling of experimental efforts with computational first-principles calculations of various reactions to determine the preferred mechanism of lithium reaction with $LaSn_3$ as well as the likely reaction products. (J. Vaughey, M. Thackeray, D. Shin, and C. Wolverton, in preparation).

In an attempt to gain insight into the electrochemical reaction of lithium with $LaSn_3$, and to determine if the reaction might form intermediate phases, Wolverton *etal* employed first-principles calculations based on density functional theory (DFT) to predict thermodynamically-preferred reactions and reaction sequences. Wolverton *etal* wish to predict low-energy reaction pathways from first-principles calculations based on density functional theory. For the $LaSn_3$ negative electrode reaction with Li, Wolverton *etal* have both considered insertion and displacement reactions. The relevant reactions that we have considered are summarized in**Error! Reference**

source not found.. ΔH_{rxn} of each reaction in **Error! Reference source not found.** is evaluated from total energies of individual phases which are obtained from VASP calculations.

Table 5. Formation enthalpies for competing reactions.

Reaction type	Reactions		ΔH (meV/Li)
Insertion	$Li + LaSn_3 \rightarrow LiLaSn_3$	(1)	864
	$12Li + LaSn_3 \rightarrow Li_{12}LaSn_3$	(2)	3232
Displacement	$66Li + 5LaSn_3 \rightarrow 5La + 3Li_{22}Sn_5$	(3)	-252
	$51Li + 4LaSn_3 \rightarrow 4La + 3Li_{17}Sn_4$	(4)	-275
	$88Li + 15LaSn_3 \rightarrow 5La_3Sn_5 + 4Li_{22}Sn_5$	(5)	-368
	$17Li + 3LaSn_3 \rightarrow La_3Sn_5 + Li_{17}Sn_4$	(6)	-395

Reactions (1) and (2) are the insertion-type reactions, starting from the vantage point of thinking of $LaSn_3$ as a structure with one of the cation sites is vacant at the body-centered position. In Reaction (1), Wolverton *etal* just filled this vacant site to form a hypothetical $LiLaSn_3$ perovskite structure. In Reaction (2), all octahedral and tetrahedral sites are filled to form a hypothetical $Li_{12}LaSn_3$ structure. Reactions (3)-(6) are displacement reactions, involving the displacement of Sn in the $LaSn_3$ structure to the most Li-rich intermediate phase in the Li-Sn system, "$Li_{4.4}Sn$". Two such phases have been reported in the literature[11, 12] for this Li-rich phase, $Li_{17}Sn_4$ and $Li_{22}Sn_5$. Wolverton *etal* considered both phases, and we considered reactions involving either La or La_3Sn_5.

In order to validate our first-principles results, the formation enthalpies of $LaSn_3$ and La_3Sn_5 are compared with experimental measurement for these compounds[13]. Figure 21 shows formation enthalpies for $LaSn_3$ and $LaSn_5$ calculated from first-principles and those from experiments and they are in good agreements.

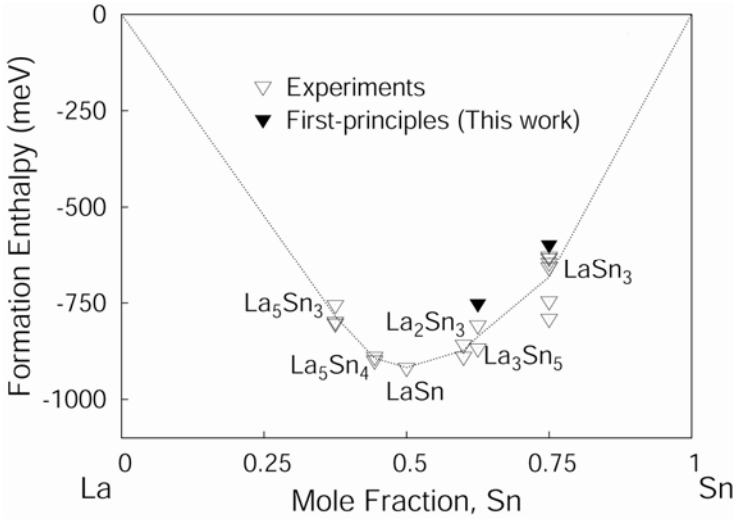

Figure 21. Calculated formation enthalpies for La_3Sn_5 and $LaSn_3$ from first-principles compared with experimental measurements (See Huang *et al.*[13] and

references therein). Dotted line represents a conceptual convex hull of La-Sn connecting averaged experimental formation enthalpies of each intermetallic compound.

Negative numbers in **Error! Reference source not found.** mean that the right-hand-side is lower in energy than the left-hand-side. It should be noted here that since our first-principles density functional calculations are those of at 0K so that temperature effect, e.g., vibrational entropy, has not been fully taken into account. However, it can be assumed that ΔS_{rxn} is almost negligible here and will not reverse the sign of above reactions. Also, the voltage of these reactions relative to Li metal is just given by $-\Delta H_{rxn}$. So, from this table, we can make the following conclusions:

(i) The insertion reactions are extremely unfavorable with a very large, negative voltage relative to Li from these calculations, and it seems extremely unlikely to occur. This can be understood by looking at $LaSn_3$: The crystal structure is commonly described as an fcc-based substitutional ordered pattern, $L1_2$. The $L1_2$ structure (prototype Cu_3Au) is one of the most common intermetallic compounds, and has 12-fold fcc-type coordination about each atom, which is close-packed. Thus, trying to insert Li into an interstitial site in a close-packed structure is going to incur a very large strain-energy penalty, and this penalty is clear from the above reaction energies.

(ii) The reactions involving $Li_{17}Sn_4$ as a byproduct are energetically more favorable than the analogous ones involving $Li_{22}Sn_5$. This essentially means that the former compound is more stable than the latter. There has been some controversy in the literature about the precise stoichiometry of this compound, and the first-principles calculations clearly indicate that $Li_{17}Sn_4$ is lower in energy than $Li_{22}Sn_5$, and thus $Li_{17}Sn_4$ is a more reasonable stoichiometry to use for the "$Li_{4.4}Sn$" phase. This result is in agreement with the x-ray and neutron work of Lupu et al.[12].

(iii) Displacement reactions involving the La_3Sn_5 phase are much more stable than those involving La. Thus, La_3Sn_5 as a product provides an energetically more reasonable pathway for the displacement reaction. The energetically preferred reaction (6) for lithiation of $LaSn_3$ from this study is a displacement reaction involving $Li_{17}Sn_4$ and La_3Sn_5 as byproducts. This reaction energy is approximately –400 meV/Li, and thus the first-principles prediction is that LaSn3 operating via this reaction sequence should have an open circuit voltage approximately 400 mV above Li. This prediction seems to be in good agreement with the measured voltage profiles, where the majority of the uptake seems to occur somewhere near ~0.5V.

Hence, for this $LaSn_3$ system, we find that DFT-GGA is quantitatively accurate. This implies that the failure of DFT in the CFx/LiF is likely specific to that system. In order to more fully address the energetics of this system, then, methods beyond DFT will need to be employed in the future.

2.3.1.2.7 Conclusions

In summary, we have used first-principles calculations based on density functional theory (DFT) to derive the open circuit voltage profiles of Li/$(CF_x)_n$ cells. Wolverton *etal* have analyzed the thermodynamics of the reaction, and assert that a stable ternary intermediate cannot reconcile the discrepancy between observed and thermodynamic calculations of the voltage. The discrepancy

could only be explained via a non-equilibrium ternary intermediate pathway. Wolverton *etal* also find that DFT is not well suited for an accurate description of the CF_x-type systems, presumably due to well-known deficiencies of DFT for treating van der Waals bonding, and molecular systems in general. Wolverton *etal* have attempted to use quantum-chemical cluster-based methods in an attempt to rectify the DFT results, without success. In an attempt to ascertain whether DFT can be accurate for other Li electrode reactions (e.g., not involving van der Waals bonding or molecular systems), we have performed studies of a recently proposed Li-ion anode material ($LaSn_3$), and find that the DFT predictions are excellent. Thus, extensions of DFT, high order quantum chemical methods, or quantum Monte Carlo based methods will presumably have to be used to study the CF_x reactions.

2.3.1.2.8 References

[1] Whittingham MS. MECHANISM OF REDUCTION OF FLUOROGRAPHITE CATHODE. J. Electrochem. Soc. 122, 526 (1975).

[2] Watanabe N. Two types of graphite fluorides, (CF)n and (C2F)n, and discharge characteristics and mechanisms of electrodes of (CF)n and (C2F)n in lithium batteries. Solid State Ionics 1, 87(1980).

[3] Kresse G, Furthmuller J. Efficient iterative schemes for ab initio total-energy calculations using a plane-wave basis set. Phys. Rev. B. 54,11169 (1996).

[4] Kresse G, Furthmuller J. Efficiency of ab-initio total energy calculations for metals and semiconductors using a plane-wave basis set. Comput. Mater. Sci. 6,15 (1996).

[5] Kresse G, Joubert D. From ultrasoft pseudopotentials to the projector augmented-wave method. Phys. Rev. B. 59,1758 (1999).

[6] Perdew JP, Chevary JA, Vosko SH, Jackson KA, Pederson MR, Singh DJ, Fiolhais C. Atoms, molecules, solids, and surfaces: Applications of the generalized gradient approximation for exchange and correlation. Phys. Rev. B. 46,6671 (1992).

[7] Monkhorst HJ, Pack JD. SPECIAL POINTS FOR BRILLOUIN-ZONE INTEGRATIONS. Phys. Rev. B. 13,5188 (1976).

[8] Pople JA, Beveridg.Dl, Dobosh PA. APPROXIMATE SELF-CONSISTENT MOLECULAR-ORBITAL THEORY .5. INTERMEDIATE NEGLECT OF DIFFERENTIAL OVERLAP. J. Chem. Phys. 47,2026 (1967).

[9] Pople JA, Gordon M. MOLECULAR ORBITAL THEORY OF ELECTRONIC STRUCTURE OF ORGANIC COMPOUNDS .1. SUBSTITUENT EFFECTS AND DIPOLE MOMENTS. J. Am. Chem. Soc. 89, 4253 (1967).

[10] Charlier JC, Gonze X, Michenaud JP. FIRST-PRINCIPLES STUDY OF GRAPHITE MONOFLUORIDE (CF)N. Phys. Rev. B. 47,16162 (1993).

[11] Gladyeshevskii EI, Oleksiv GI, Kripyakevich PI. New Examples of the Structural Type Li22Pb5. Sov. Phys. - Crystallogr. 9, 269 (1964).

[12] Lupu C, Mao JG, Rabalais JW, Guloy AM, Richardson JW. X-ray and neutron diffraction studies on "Li4.4Sn". Inorganic Chemistry 42, 3765 (2003).

[13] Huang MW, Su XP, Yin FC, Zhang P, Li Z, Chen CT. A thermodynamic assessment of the La-Sn system. Journal of Alloys and Compounds 309,147 (2000).

3. Published work related to this LDRD

1) H. F. Hunger and G. J. Heymach, J. Electrochemical Soc. 120, 1161(1973) and references therein. (This describes the discharge characteristics of CFx material)

2) H. Gisser, M. Petronio and Shapiro, Lubric Eng. 28, 161(1972) and references therein. (This describes the discharge characteristics of CFx material)

3) N. Watanabe, Solid State Ionics 1, 87(1980). (This paper describes two types of graphite fluoride, their discharge characteristics etc).

4) M. S. Whittingham, J. Electrochemical Soc. 122, 526(1975).
(This paper describes the ternary intermediate compound that determines the cell OCV)

5) M. A. Rodriguez, D. Ingersoll, and D. H. Doughty, Powder Diffraction, 18, 135(2003)

4. Conclusions

In this section we describe the main conclusions of our study in the last three FYs.

1. We developed methodology to coat $(CF_x)_n$ electrodes that exhibited:
    - Uniform loading
    - Reproducible and optimized performance
2. Performed In-situ x-ray studies while the pouch cell was discharging:
    - Collected X-ray data continuously till the cell is finished
    - Performed Multivariate Analysis on the X-ray data and identified the presence of an intermediate in the discharge reaction. Although others have speculated the presence of an intermediate we have shown that the intermediate does exist in the discharge reaction.
3. After successfully identifying the presence of the intermediate we moved forward with identifying the nature of the intermediate species with modeling.
    - Molecular Dynamic Simulation
    - Density Functional Theory
4. Finally, the electrode coating and cell fabrication expertise gained in this project has promise to bring-in funding from out-side sources including private companies both domestic and foreign.

5. R&D Needs and Opportunities

The author has identified the following activity as potentially fruitful research addressing the key issue of increasing the operating voltage in order to double the exchange interval time of the LLC. At Sandia National Laboratories we have identified the presence of the intermediate in the $(CF_x)_n$ discharge reaction by in-situ x-ray studies while the cell was being discharged. The two modeling studies also confirmed the existence of the intermediate. The next logical step in the evolution of this study is to prevent the formation of the intermediate by appropriately modifying the $(CF_x)_n$ structure by doping with a foreign atom, for example, nickel, cobalt, or chromium. This approach we believe will introduce ensemble of energy level in the $(CF_x)_n$ lattice which matches that of the intermediate. This could either eliminate formation of the intermediate or provide a pathway to mitigate the effect of the intermediate. So the choice of the dopant is critical to eliminating the deleterious effect of the intermediate. Using Computer Modeling Capabilities in Org 6316 the choice of the dopant can be determined. Once this is accomplished, for the final demonstration, the material will be synthesized by a private company (there is a private company in Tulsa, OK which is dedicated to the production of $(CF_x)_n$ primarily for US customers) and tested in cells at Sandia National Laboratories.

The development of this in-house capability has generated interest in the private companies in the US and abroad. This awareness is bringing in research opportunities through WFOs. We will take advantage of this awareness and elevate this SNL capability to a higher level to prepare NW quality power sources for future NW applications.

Appendix A

Int. J. Electrochem. Sci., 2 (**2007**) 913 - 922

International Journal of
ELECTROCHEMICAL
SCIENCE
www.electrochemsci.org

Fabrication and Testing Capabilities for 18650 Li/$(CF_x)_n$ Cells

Ganesan Nagasubramanian[*]

2546 Advanced Power Sources R & D Department Sandia National Laboratories 1515 Eubank SE Albuquerque, NM 87185, USA
[*]E-mail: gnagasu@sandia.gov

Received: 25 July 2007 / *Accepted:* 30 August 2007 / *Online published:* 20 October 2007

Sandia National Laboratories has world-class facilities for building and testing lithium and lithium-ion batteries. In this article we describe the in-house facilities for fabricating electrodes and cells in detail. Our in-house facility includes equipment for: 1) electrode coating, 2) electrode slitting, 3) electrode winding, 4) cell grooving, 5) electrolyte filling, 6) cell crimping and more. We also have a 48-channel Maccor tester and several impedance units for electrochemical characterization. These facilities provide flexibility for cell fabrication techniques which in turn allows us to continually improve cell performance. Under an internally funded program we are developing in-house capability to fabricate and evaluate 18650 Li/$(CF_x)_n$ cells using "Li-ion" electrode fabrication methodologies to prepare the thin film $(CF_x)_n$ electrodes. At a C/400 discharge rate cell delivered ~3.6 Ahrs capacity. We also evaluated cathodes of two different lengths for uniformity of loading. The loading along the electrode length was found to be extremely uniform, as the delivered capacity was proportional to cathode length. For example, a 0.91 meters long x 4.2 mil thick electrode gave 3.6 Ahrs capacity while a 0.72 meters long x 4.2 mil thick electrode (19.4% less length) gave 2.9 Ahr of capacity (19.4% less capacity). We also discharged the cells with 0.71 meters long electrodes at different temperatures. The cells delivered practically the same capacity over temperatures from 25 to 72°C. At -20°C the cells delivered 81% of the room temperature capacity at a C/200 rate; however, at -40°C the cells delivered close to 47% of the room temperature capacity under similar test conditions. The performance behavior of 18650 cells will be discussed in more detail in the paper.

Keywords: $(CF_x)_n$ = Carbon Monofluoride; capacity; self-discharge; PVDF; electrical testing; primary battery

1. INTRODUCTION

Sandia National Laboratories (SNL) has responsibility for the design and production of several power sources required to serve the national interest. SNL also maintains extensive research and development facilities in support of these activities. As a result, SNL has invested $10s of millions

over the past decade to develop infrastructure related to all aspects of power source development and production. This Section motivates the work performed on $Li/(CF_x)_n$ electrodes fabricated in-house, while Section 2 describes the resources available in-house that are specific to fabrication of Li-ion and $Li/(CF_x)_n$ chemistries. The single cell performance test results are provided in Section 3, and the paper is summarized in Section 4.

Interest in the $Li/(CF_x)_n$ chemistry is burgeoning lately for applications requiring long life, light weight and very low self-discharge because it yields the highest theoretical specific energy of any lithium primary chemistry (see Table 1). Self-discharge is on the order of <0.5 % per year near room temperature (1). These and other positive attributes such as its small voltage delay, cell safety, and lower weight* are expanding interest in this chemistry into new application areas. For example, the US Army is looking into the possibility of using $Li/(CF_x)_n$ cells to meet Land Warrior and Dismounted Soldier power requirements (2). Other US government organizations such as NASA and the CIA are considering this technology for celestial and terrestrial applications, respectively. In many of applications, battery safety is critical, as in confined areas such as in submarines. The US Navy evaluated the safety of the $Li/(CF_x)_n$ cells for the Navy use. According to US Navy 9310 Safety Testing, $Li/(CF_x)_n$ batteries under specified electrical abuse test conditions produced benign results (3).

Table 1. Comparison of theoretical and practical energy values for the four Li primary chemistries.

Chemistry	Voltage (V)	Specific Energy (Whr/kg)	
		Theoretical	Practical
$LiCF_x$	3.2	2.260	220
$LiMnO_2$	3.0	1.005	200-270
$LiSOCl_2$	3.6	1.470	430
$LiSO_2$	3.0	1.170	240

Even with all these favorable characteristics, however, this chemistry has been unsuccessful in challenging other primary chemistries in terms of commercial market penetration. For over 30 years $Li/(CF_x)_n$ has been resigned to low-current drain applications due to its poor performance at low temperatures and high discharge rates. For example, the practical capacity for this chemistry is only ~10% of the theoretical at moderate discharge rates (see Table 1). We hypothesized that these problems are aggravated partly by the use of thicker electrodes (> 40 mil thick) which contain Teflon as a binder material. The use of thick electrodes and larger amounts of electrically insulating binder materials increases the series resistance and concomitant IR drop inside the battery, which results in the precipitous drop in capacity at lower temperatures. Thinner electrodes are not currently commercially fabricated because there is no commercial need for cells with improved low temperature performance.

* Typically a 4-Ahr 18650 $Li/(CF_x)_n$ cell weighs ~28 grams which is ~ 14 grams lower than the weight of a 2.5-Ahr same size Li-ion cell.

In order to test this hypothesis, we have leveraged Sandia's capabilities in fabricating Li-ion cells with thinner coatings to address this problem by fabricating thinner electrodes. We fabricated $(CF_x)_n$ electrodes 4.2 mil (0.1 millimeters) thick (10x thinner than current standard commercial technology) and measured the discharge performance at low temperatures, which will be described in Section 3. The extensive facilities described in Section 2 below have allowed us to adapt and fine-tune Li-ion methodologies to prepare and tailor the properties of thin film $(CF_x)_n$ electrodes as desired. Without these facilities we would have been forced to depend on commercial battery manufacturers where the freedom of doing basic research and development on this important chemistry would have been severely restricted.

2. FABRICATION OF $(CF_x)_n$ 18650 CELLS USING SNL's IN-HOUSE FACILITIES

In previous Li-ion cell work, two different PVDF binders had been used. Kureha W#1300 was used to bind the cathode material, while Kureha W#9200 was used for the anode. In the case of Li/$(CF_x)_n$ cells, the anode is metallic lithium, and does not require a binder. Since $(CF_x)_n$ is a cathode material, the first thought for choice of binder would be the Kureha W#1300. On the other hand, Kureha W#9200 might also be a good choice, since one of the discharge products of this chemistry is carbon. It was not clear initially which one of the binders was likely to work better for the $(CF_x)_n$ based on the Li-ion work. Therefore electrodes were prepared using each binder and tested in a single cell configuration. The electrical data suggested that the Kureha W#9200 binder may be more suitable, and thus was used in the experiments described below. The inferior performance of cells with W#1300 binder might have come from the poor adhesion of the active material to the electrode. Electrodes were coated on both sides of an aluminum current collector (12 microns thick) with a 3 micron carbon coating on each side (InteliCoat, South Hadley, MA, USA). We found that a thin coating of carbon is necessary to promote adhesion of the $(CF_x)_n$ onto the Al current collector.

2.1. Recipe for making slurry for the $(CF_x)_n$ cathode

The properties of the slurry, particularly the viscosity and particle size, greatly impacted the quality of the electrode and subsequent electrochemical performance. Slurries were made with extreme care to achieve the properties necessary for making reproducible electrodes. The slurry was prepared on a BYK AE High Speed Dissolver Dispermat AE1-M. Typically, 7.5 gm of PVDF was dissolved in 200 ml of N-Methyl-2- Pyrrolidinone (NMP). To this solution were added 7.5 gm of acetylene black and 50 ml additional NMP, and the mixture was stirred for 20 minutes. Finally, 135 gm of $(CF_x)_n$ were added and the mixture was stirred at 3200 RPM for 1hour. The viscosity of the slurry was measured to be between 230-240 cP using a BYK-Gardner USA Cap Viscometer, Model# Cap 2000+. The aggregate particle size of the slurry was measured using a Hegman-Fitness-of-Grind gage. The optimum aggregate particle size of the slurry was typically around 3-5 microns, which we found to be ideal for fabrication of reproducible electrodes. Typical optimized slurry composition was 90 w% $(CF_x)_n$, 5w% PVDF, and 5 w% acetylene black.

2.2. $(CF_x)_n$ Electrode Coating

A Hohsen (Osaka, Japan) Electrode Coater, shown on the right, was used to apply and heat-treat coatings. The oven was preheated to 130°C to evaporate off the NMP solvent. The as-coated cathodes were ~130 mm wide and several meters long. Typically the active material coatings were 2.1 mils thick on each side of the current collector. The average total electrode thickness of the dry electrode was around 4.9 mils (including the current collector). Prior to rolling, the electrode was cut to length by hand and then slit the 130 mm to 50 mm wide in a Hohsen slitter (not shown). The electrode was baked at 100°C overnight and kept in a dry room (dew point -40°C or better).

Photo 1. Hohsen Electrode Coater

2.3. Anode

For 18650 cells, thin lithium electrodes specially made with copper cladding are employed as the anode (Furukawa, Japan). The copper is 8-10 microns thick with a 20-micron Li film vapor deposited on each side (see Photo 2). The Cu cladding was necessary to withstand the tension applied while winding the cell. A nickel tab was normally cold-welded to the anode before winding.

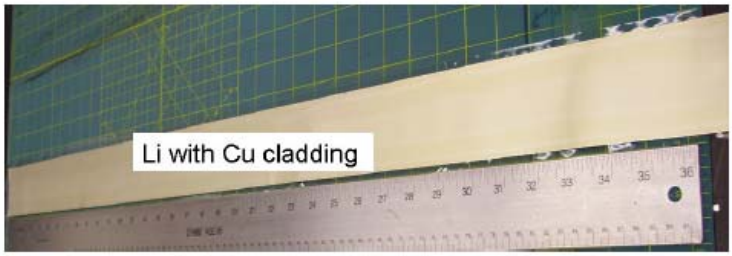

Photo 2. Li electrode with Cu cladding

2.4. Cathode

The photo on the right (Photo 3) shows the $(CF_x)_n$ electrode coated at Sandia. This electrode has been cut to length, slit to width and baked at 100°C overnight. After baking the electrodes remain in a dry room (dew point -40°C or better).

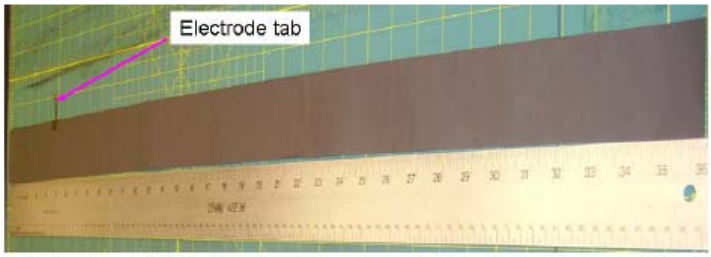

Photo 3. SNL $(CF_x)_n$ electrode with tab welded ultrasonically

2.5. Ultrasonic Welding

Before attaching the current collector tab to the cathode, a small area (2mm x 5mm) of the coating was dissolved using NMP as the solvent approximately 10 cm from one end of the electrode. The area was wiped clean of any residue before baking again in vacuum at 100°C overnight in a National Appliance Company Vacuum Oven (Model #5861). Finally, the tab was attached for electrical contact (see photo 4) using an Ametek Ultrasonic Welder.

Photo 4. Amtech Ultrasonic Welder

2.6. Cell Winding

The photo 5 on the right shows a semi-automatic Hohsen winder that we used for winding cell rolls. For the 18650 cells 54-mm wide anodes, 50-mm wide cathodes, and 58-mm wide Celgard (North Carolina, USA) 2325 separators were used. Since the anode is on the outside of the roll it is longer

than the cathode by about 4-5 cm. Initially we were building cells that have typically 0.91 meters long cathode electrodes.

Recently we started using a new semi-automatic winder from Hohsen (photo 6). This machine can take a maximum electrode length of only 0.81 meters which is 10 cm shy of the other machine described above. The capacity of 18650 cells made with this winder is somewhat less (around 3 Ahr).

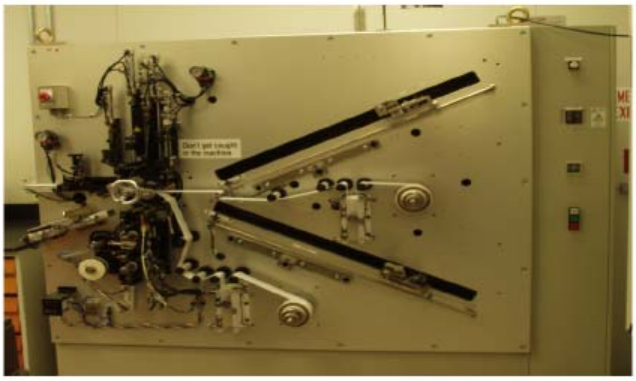

Photo 5. Cell Winder for winding cell rolls for 18650 cells

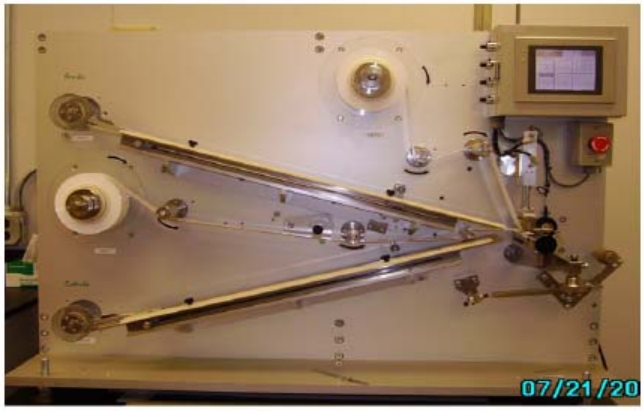

Photo 6. Hohsen manual winder

2.7. Cell Grooving

The anode tab was spot-welded to the bottom of the 18650-can through the central mandrel hole and the can was grooved just above the roll to prevent the roll from sliding out of the can. The cell grooving was accomplished using the machine shown in photo 7. After grooving, the header (consisting of a burst disc, polypropylene-type cup, Ni washer as replacement for the PTC current

controlling device) was attached to the cathode tab using the Amtech ultrasonic welder described above.

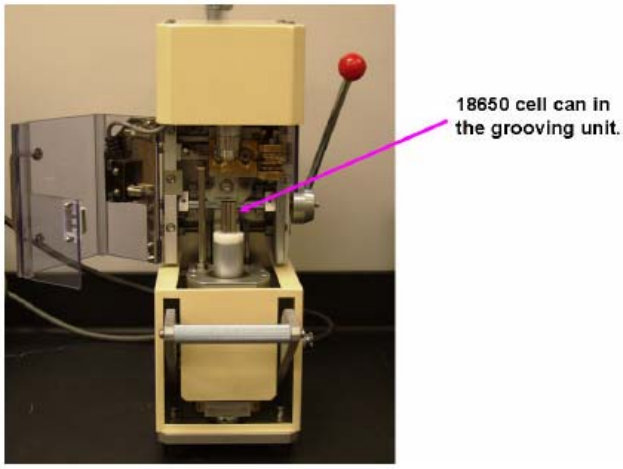

Photo 7. Cell Groover

2.8. Cell Filling and Crimping

After attaching the header, the cells were moved into an Argon atmosphere glove box for electrolyte filling and crimping. Cells took approximately 3.2 ml of electrolyte. After filling, the cells were crimped and the open circuit voltage was measured to insure against shorting. Before testing for capacity or impedance, the cells were kept at 40°C overnight to allow for soaking of the electrolyte into the cathode bulk. A finished cell is shown below in photo 8.

Photo 8. SNL-Built 18650 Li/$(CF_x)_n$ Cell

3. RESULTS AND DISCUSSION

The 18650 cells were evaluated for capacity at different temperatures in EC:PC:EMC (1:1:3 w%)- 1 M $LiBF_4$ (Sandia Electrolyte, "SNL-E"). The ionic conductivity of SNL-E is ~4-5 mS/cm at and near room temperature.

3.1. Improvement in Delivered Capacity in 18650 cells

Figure 1 shows the evolution of delivered capacity in 18650 cells. The cells compared in Figure 1 all have 0.91 meters long cathodes. Although the initial capacity was around 1.5 Ahrs, the delivered capacity increased to 3.6 Ahrs by optimizing the electrode quality, thickness etc. The key to improving the discharge capacity of the cell was found to be related to the rheology of the cathode slurry. The process of optimization of properties of the slurry, such as the viscosity, aggregate particle size, etc. took several iterations to obtain the optimum mix of properties. The slurry that repeatedly gave the best performance had a viscosity of ~230 cP and an aggregate particle size of <5 µm.

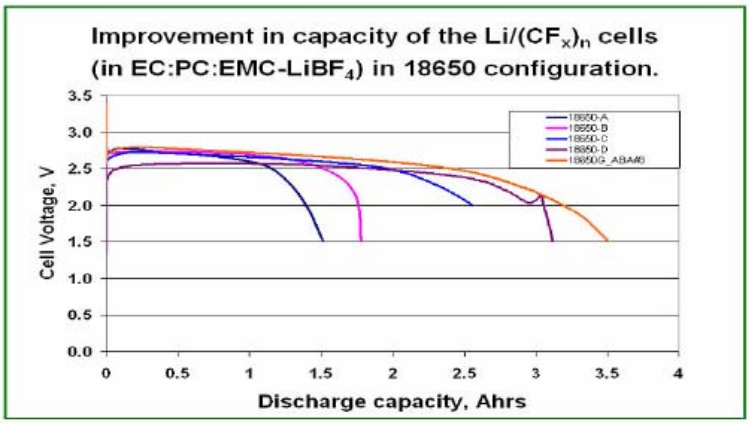

Figure 1. Improvement in 18650 cell capacity obtained at 25°C in SNL-E

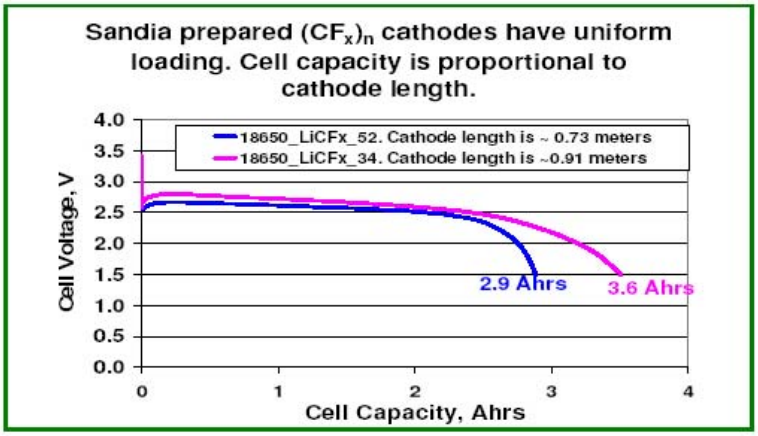

Figure 2. compares the discharge capacity of these cells discharged at 10 mA.

We also checked for uniformity of electrode loading across the length of the electrode. We made 18650 cells with cathodes of different lengths (0.91 and 0.81 meters).

The discharge capacity was found to be proportional to the cathode length. The longer electrode (0.91 meters gave 3.6 Ahrs and the shorter (0.81 meters long) 2.9 Ahrs. The 19.4% reduction in length resulted in a 19.4% reduction in capacity indicating that the full electrode length was active in the cell. In addition, the operating voltage for the cell with shorter electrode is slightly lower than that with the longer electrode. This is expected since for the same discharge current (10 mA), the current density is higher for shorter electrode (13.6 $\mu A/cm^2$) than for the longer electrode (10.9 $\mu A/cm^2$).

3.2. Temperature Performance

We also evaluated the discharge capacity of cells at different temperatures. The cells were discharged at a 15 mA current. No change in delivered capacity was observed in the temperature regime from 25 to 72°C. At -20°C, however, the cells only delivered 81% of the room temperature capacity, while at -40°C the cells delivered close to 47% of the room temperature capacity. These results are significant in comparison to the performance of the commercial cells at low temperatures. Recall that at low temperatures commercial $(CF_x)_n$ cells deliver <10% of the room temperature capacity.

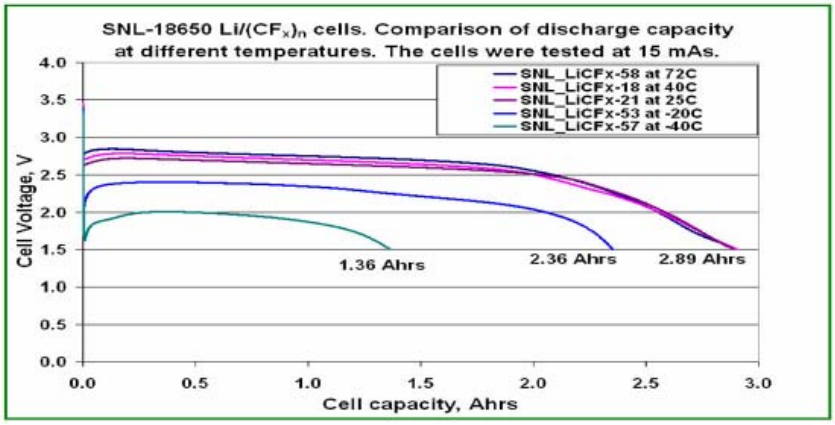

Figure 3. Discharge capacity at different temperatures

4. SUMMARY

The goal of this work is to produce a robust Li/$(CF_x)_n$ battery for Sandia internal applications. Sandia National Laboratories has invested in developing a large infrastructure to address power source R&D problems for niche applications. We have successfully demonstrated the adaptation of Li-ion electrode preparation methodologies to $(CF_x)_n$ electrode fabrication. A suitable binder material (Kureha W#3200) was identified for use as a cathode binder material. 18650 cells were fabricated in-house using SNL-prepared electrodes. Several different combinations of electrode compositions, thicknesses, binder materials, etc. were evaluated to develop electrodes with reproducible behavior. We showed that the electrodes have uniform loading across the electrode length. We obtained as high

as 3.6 Ahr capacity in 18650 cells. We also measured cell capacity at different temperatures. Between 72 and 25°C the discharge capacity was essentially the same. At -20°C, the capacity dropped to 81% of the room temperature value, and at -40°C it decreased to 47%, which represents about a five-fold improvement over current state-of-the-art of commercial cells. We will continue our efforts to improve the low temperature performance by minimizing the impedance, improving the thermal stability, etc by fine-tuning the chemistry.

ACKNOWLEDGMENT
Sandia is a multiprogram laboratory operated by Sandia Corporation, a Lockheed Martin Company for the United States Department of Energy's National Nuclear Security Administration under contract DE-AC04-94AL85000. The author would like to thank Lorie Davis for preparing and testing cells. Also, the author would like to thank Karen Waldrip for her comments on the content of the paper and editing the manuscript.

References

1. Handbook of Batteries 2nd Edition, David Linden, Editor: McGraw Hill, New York, p14.68, 1998.
2. Arek Suszko, RDECOM, CERDEC, Army Power Division, Fort Monmouth, NJ personal communication.
3. US Navy Technical Manual , S9310-AQ-SAF-010 issued on August 19, 2004

Appendix B

electronic reprint

Journal of
Applied
Crystallography
ISSN 0021-8898
Editor: Gernot Kostorz

In situ X-ray diffraction analysis of $(CF_x)_n$ batteries: signal extraction by multivariate analysis

Mark A. Rodriguez, Michael R. Keenan and Ganesan Nagasubramanian

Journal of
Applied
Crystallography

ISSN 0021-8898

Received 6 March 2007
Accepted 27 August 2007

In situ X-ray diffraction analysis of $(CF_x)_n$ batteries: signal extraction by multivariate analysis

Mark A. Rodriguez,* Michael R. Keenan and Ganesan Nagasubramanian

Sandia National Laboratories, Albuquerque, NM 87185-1411, USA. Correspondence e-mail: marodri@sandia.gov

$(CF_x)_n$ cathode reaction during discharge has been investigated using *in situ* X-ray diffraction (XRD). Mathematical treatment of the *in situ* XRD data set was performed using multivariate curve resolution with alternating least squares (MCR–ALS), a technique of multivariate analysis. MCR–ALS analysis successfully separated the relatively weak XRD signal intensity due to the chemical reaction from the other inert cell component signals. The resulting dynamic reaction component revealed the loss of $(CF_x)_n$ cathode signal together with the simultaneous appearance of LiF by-product intensity. Careful examination of the XRD data set revealed an additional dynamic component which may be associated with the formation of an intermediate compound during the discharge process.

1. Introduction

1.1. *In situ* X-ray diffraction analysis

The use of *in situ* X-ray diffraction (XRD) analysis has proved to be a powerful method for analysis of materials with application to the battery industry (Chartouni & Gross, 2001; Hatchard & Dahn, 2004; Reimers & Dahn, 1992; Rodriguez *et al.*, 2000). Past work focused on XRD measurements of relatively sharp diffraction peaks from well crystallized materials assembled into reaction cells with X-ray windows (*e.g.* beryllium, plastic *etc.*). While peak overlap from scattering of the cell materials often occurred in these cases, it was still possible to derive useful information associated with the dynamic reactions occurring during charge/discharge cycles of these electrochemical cells simply by ignoring the overlap regions. However, analysis of weakly scattering and/or nanocrystallite-size materials can prove difficult as the dynamic signal from the chemical reaction is often lost among the scattering of the inert parts of the fabricated *in situ* electrochemical cell. The compound $(CF_x)_n$ epitomizes the challenges of weak X-ray scattering and broad diffraction profiles that hinder *in situ* analysis. We present results that illustrate how this difficulty can be overcome by the use of multivariate analysis (MVA). The mathematical treatment of data sets by MVA aids in the extraction of weak signals. We present our findings in the context of our *in situ* XRD analysis of a $Li/(CF_x)_n$ electrochemical cell.

1.2. Motivation

Lately there has been growing interest in improving the performance of $Li/(CF_x)_n$ cells for space and military applications. Of all the known ambient-temperature Li-primary chemistries, $Li/(CF_x)_n$ has the highest theoretical specific capacity and energy. However, the practical energy is only 10–35% of the theoretical value depending on the discharge rate and cell size (Nagasubramanian & Rodriguez, 2007). One of the reasons for the poor performance is the low operating cell voltage (~2.5 V), which is much lower than the open circuit voltage of ~3.4 V. The consensus in the scientific community is that an intermediate species (in the discharge reaction) is responsible for the depression in the operating voltage. During the 1970s and 80s, several researchers proposed reaction schemes, but without irrefutable proof for their hypotheses. For example, Hagiwara *et al.* (1988), on the basis of their analyses of discharge products and open circuit voltage (OCV) measurements in different solvents, proposed that the discharge reaction includes electrochemical formation of an intermediate phase comprising Li^+, (CF) and a solvent molecule, followed by the subsequent chemical decomposition of the intermediate to the final products. However, there was no proof for the existence of the intermediate species. Whittingham (1975) proposed that a ternary nonstoichiometric intercalation compound of the type $(CLi_xF)_{x<1}$ (formed in the discharge reaction) determined the OCV of the cell. He also suggested that when $(CF_x)_n$ is chemically reduced, its interplanar spacing expands to 9.35 Å. However, this type of lattice expansion could not be confirmed in an electrochemically reduced material. Clearly, $(CF_x)_n$ poses significant challenges with regard to understanding its behavior during the electrochemical reaction process. We have been applying *in situ* XRD measurements to the $Li/(CF_x)_n$ battery system for the purpose of understanding the discharge reaction mechanism, and ultimately propose solution(s) for increasing the operating voltage close to 3.0 V at moderate discharge rates. The innovative mathematical treatment of the XRD data set using a technique of multivariate analysis significantly aided data reduction and analysis and is the focus of this manuscript.

2. Methods

2.1. *In situ* cell design

We have previously developed a method for *in situ* XRD analysis of 'pouch' cells (Rodriguez *et al.*, 1998, 2000) for the purposes of obtaining information on the structure/property relationships regarding battery systems. In the pouch technique, a functional cell (cathode, separator, anode, electrolyte *etc.*) is assembled within a very thin plastic bag and then vacuum-sealed in such a way as to allow the electrode leads to exit the sealed pouch. Sufficient penetration of X-rays through the low atomic number (*i.e.* low-Z) materials that make up the pouch cell allows scrutiny of structural changes occurring within the anode and/or cathode as the functional cell is discharged. We employed this pouch-cell technique to analyze the $(CF_x)_n$ cathode material as a function of discharge. Our *in situ* (pouch) cell design for the $(CF_x)_n$ battery was very similar to cells designed in the past for Li-based intercalation compounds (Rodriguez *et al.*, 1998, 2000) and we refer the reader to that work for details regarding cell construction. In brief, the cathode was prepared by depositing $(CF_x)_n$ mixed with binder onto a thin (25 µm) Al current collector. The cell was assembled using an Li metal anode (~100 µm thickness), a Celgard 2325 cell separator (25 µm thickness) and a $(CF_x)_n$ cathode (~100 µm thickness). The supporting electrolyte solution used was 1.2 molar $LiPF_6$ in ethylene carbonate/ethyl methyl carbonate (30:70 wt%). The constituent parts were assembled into a stack, placed within a small plastic pouch (25 µm thickness polypropylene) and sealed by impulse heating. The cell was then vacuum-filled with the electrolyte through a small fill-hole left in the cell, allowed to soak (~5 min) and then sealed while a vacuum was applied to optimize compression of the cell components.

2.2. *In situ* XRD data collection

XRD data collection *via* the pouch cell has been outlined previously (Rodriguez *et al.*, 1998, 2000). Briefly, XRD patterns were collected using a Siemens automated θ–θ powder diffractometer equipped with Cu $K\alpha$ radiation, a diffracted-beam graphite monochromator, and a scintillation counter. The *in situ* pouch cell was connected *via* lead wires to a computer-controlled potentiostat. The *in situ* cell was discharged at a rate of C/72 (*i.e.* capacity of cell/hours). Parameters for typical XRD scans were a 5–80° 2θ range, a 0.05° 2θ step size and a count time of 2.3 s per step (~1 h per scan). The entire experiment took ~55 h. One notable deviation of this experiment from previous work was that the XRD data collection was performed with the pouch cell inverted so that the Li anode faced the incident X-ray beam. In the $(CF_x)_n$ pouch-cell design, the $(CF_x)_n$ cathode was coated on only one side of the Al current collector and this side faced the separator. Hence, exposure of the cathode side of the pouch cell to the X-ray beam would necessitate that the beam penetrate through both the outer plastic bag and the Al to obtain a signal from the underlying $(CF_x)_n$. The Al layer proved too absorbing of X-rays to obtain sufficient signal from the $(CF_x)_n$ cathode. Fortunately, by exposing the anode side of the pouch cell to the X-ray beam, it was possible to observe diffraction from the $(CF_x)_n$ cathode by penetrating through the outer bag, the Li anode and the cell separator to the $(CF_x)_n$ cathode underneath. The drawback to this method was that the XRD patterns were complicated by signals from all of these cell layers.

2.3. Preliminary discussion of observed XRD patterns

It is useful at this point to present the initial appearance of the X-ray diffraction pattern obtained from just the $(CF_x)_n$ material as it compares with the fully assembled pouch cell. This discussion helps to clarify some of the difficulties posed by the *in situ* analysis, as well as shed light on the process of data treatment *via* MVA. Fig. 1(*a*) shows a diffraction pattern of the $(CF_x)_n$ material pressed into a bulk sample. Also plotted on this figure is the initial XRD pattern of the *in situ* pouch cell prior to discharge (Fig. 1*b*). Although the $(CF_x)_n$ pattern (Fig. 1*a*) shows broad reflections typical of the $(CF_x)_n$ material (Watanabe, 1980), the $(CF_x)_n$ peaks can still be clearly observed. In contrast, the appearance of the initial XRD pattern for the fully assembled pouch cell (Fig. 1*b*) shows a very complicated pattern due to the diffraction peaks associated with the various parts of the cell (*i.e.* the separator, plastic bag, Li anode and Al current collector). Identification of the many other peaks observed in Fig. 1(*b*) was straightforward as various parts of the pouch cell were run individually to identify their diffraction signatures. With regard to the $(CF_x)_n$ material within the pouch cell, the only detectable $(CF_x)_n$ peak in Fig. 1(*b*) is a shoulder observed on the low-angle side of the first separator peak (labeled as CFx in the figure). Such a pattern demonstrates the considerable challenges associated with this XRD analysis. It is important to point out that the peaks observed in Fig. 1(*b*) can be easily identified as being associated with a specific part or parts of the *in situ* pouch cell. This becomes important during the MVA treatment of the data set as discussed below. Also note

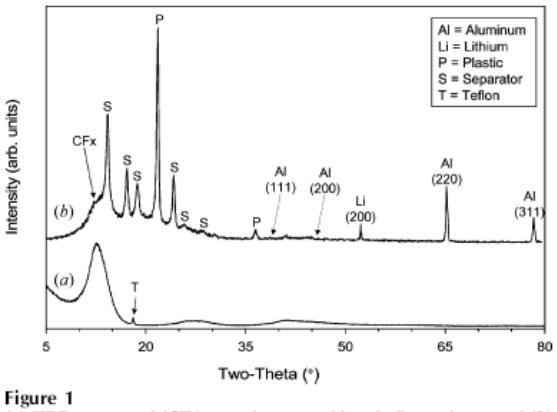

Figure 1
(*a*) XRD pattern of $(CF_x)_n$ powder pressed into bulk specimen, and (*b*) pattern obtained from pouch cell prior to *in situ* discharge. Note that the appearance of the pouch-cell pattern is complicated by the many constituents within the cell.

that the Al (111) and (200) peaks (dashed arrows) are not detected above the background in Fig. 1(*b*). This will also be addressed later.

3. Multivariate statistical analysis (MVA)

3.1. Overview

Multivariate statistical analysis provides a powerful set of tools for extracting chemically interesting information from complex, noisy data sets. Our application of MVA is based on the principle of superposition. Specifically, we assume that each observed diffraction pattern can be described as a linear combination of the patterns arising from all of the diffracting species present in the sample. In mathematical terms

$$\mathbf{Y} = \mathbf{A}\mathbf{X}^{\mathrm{T}} + \mathbf{E},$$

where $\mathbf{Y}$ is an $m \times n$ matrix containing m measured diffraction patterns, each recorded at n values of 2θ, $\mathbf{X}$ is an $n \times p$ matrix of the diffraction patterns corresponding to the p pure components present in the sample, and $\mathbf{A}$ is an $m \times p$ matrix of abundances that describes the contribution that each of the p diffracting components makes to the m observed patterns. $\mathbf{E}$ is a matrix of experimental errors assumed to be random with zero mean, and the superscript T represents the matrix transpose. It is important to note that the term 'pure component' may refer either to a single phase or to a collection of phases that vary together in a systematic way. The problem posed by the equation is twofold. First, the number of independently diffracting components to include in the analysis needs to be determined, and second, the data matrix must be factored. As the equation is a single matrix equation in two unknowns, it does not admit a unique solution. Thus, in our forthcoming treatment of the observed XRD data set presented herein, we attempt to find a representation that allows the component matrices to be most easily interpreted in physical terms.

3.2. Principal component analysis (PCA)

Our initial treatment of the XRD data set employed principal component analysis (Jollife, 2002). PCA is probably the most ubiquitous and familiar tool of multivariate analysis. PCA is typically used to reduce the dimensionality of large data sets, retaining as much information as possible while excluding noise. An application of PCA for the purpose of noise-removal from XRD data has been described recently by Chen *et al.* (2005). PCA begins by finding that single direction in the multidimensional space that best accounts for the variation in the data. This is the first principal component. The second principal component is that direction, orthogonal to the first, that best accounts for the remaining variation. This process can be continued until the desired number of principal components is computed, with each component being orthogonal to all of the preceding ones. In traditional spectroscopic usage, the columns of the $\mathbf{X}$ matrix are termed the loading vectors, and they describe, in this case, the diffraction characteristics of the pure components. The columns of $\mathbf{A}$ are then called the scores, and they describe the distributions of the respective components.

PCA has a close connection to eigenanalysis, and the eigenvalues of the data cross product matrix $\mathbf{Y}^{\mathrm{T}}\mathbf{Y}$ can be used to estimate the number of chemically relevant components embodied in the data (Malinowski, 1987). For the case that the experimental error is uniform, namely, that the size of the error is independent of the magnitude of the signal, all of the eigenvalues representing noise should be equal when weighted by the degrees of freedom used in their determination. Real systematic variation adds to any noise that is collinear with it, increasing the corresponding eigenvalue. Thus, a strategy for determining the number of pure components is to examine a plot of the sorted eigenvalues and find the break in the curve. The situation is somewhat complicated in the case of XRD data because the noise is not uniform but rather is dominated by counting statistics. However, procedures for scaling the data to account for this Poisson noise have been detailed previously by Keenan & Kotula (2004*a*,*b*). The eigenvalue plot corresponding to the scaled *in situ* cell XRD data set is shown in Fig. 2. It is evident from the plot that systematic variation in the data can be described by four components.

The p-component PCA description of a given data set has the virtue of providing the best fit to the data, in a least-squares sense, of all possible p-component models. One shortcoming, on the other hand, is that orthogonality conditions imposed by PCA have no basis in physical reality. Consequently, the principal components are often abstract representations of the chemical information and not easily interpreted. Fig. 3 displays the four most significant principal components for the XRD data set. The first loading vector resembles the mean diffraction pattern and has a relatively constant intensity as a function of time. This component primarily describes how the fixed constituents of the *in situ* cell diffract. The time-varying reaction behavior is largely contained in the second principal component. Interestingly, the disappearance of $(CF_x)_n$ and appearance of LiF peaks

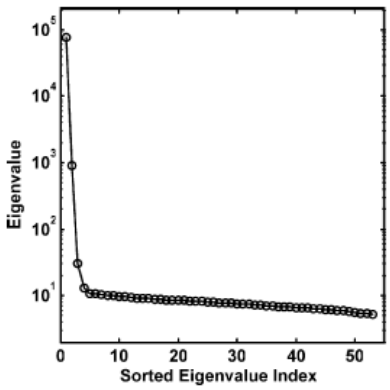

Figure 2
Sorted eigenvalues of the XRD data cross product matrix obtained after scaling the data to account for Poisson noise.

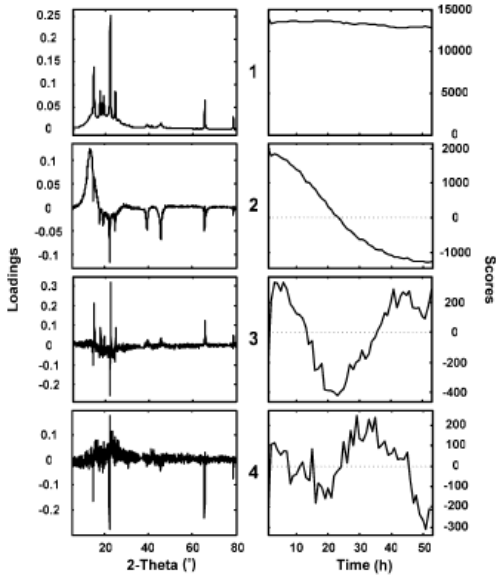

Figure 3
The first four principal components of the *in situ* cell XRD data set derived using PCA.

share the same time dependence. In the latter case, the appearance of LiF is inferred from an increasingly negative amount of a negative feature. The interpretations of the final two principal components are not as clear, although the derivative shapes in loading vector 3 are suggestive of slight 2θ-axis shifts.

3.3. Multivariate curve resolution with alternating least squares (MCR–ALS)

There are many approaches to obtaining more easily interpreted pure components. Principal components can be 'rotated' in a variety of ways to increase their simplicity. Such rotations are a staple of factor analysis and many specific methods, such as the popular varimax rotation, have been described by Harman (1976). Other approaches include alternating least-squares-based multivariate curve resolution (MCR–ALS) (Tauler *et al.*, 1993), which we have previously applied to energy dispersive X-ray spectral images (Kotula *et al.*, 2003). MCR–ALS proceeds by solving a sequence of conditional least-squares problems subject to physically appropriate constraints. For example, given an initial estimate of one of the component matrices, $\mathbf{X}$, for instance, $\mathbf{A}$ and $\mathbf{X}$ can be estimated by iterating

$$\mathbf{A} \leftarrow \min_{\mathbf{A}|\mathbf{X}} \left\| \mathbf{Y} - \mathbf{A}\mathbf{X}^{\mathrm{T}} \right\|_{\mathrm{F}}^{2} \quad \text{subject to contraints on } \mathbf{A}$$

$$\mathbf{X} \leftarrow \min_{\mathbf{X}|\mathbf{A}} \left\| \mathbf{Y} - \mathbf{A}\mathbf{X}^{\mathrm{T}} \right\|_{\mathrm{F}}^{2} \quad \text{subject to contraints on } \mathbf{X}$$

until an acceptable level of convergence is achieved. The Frobenius norm, which is the sum of all the squared residuals, is the criterion minimized at each step. For the analysis presented here, the MCR–ALS iteration was initialized with the observed diffraction pattern from the last time step (*i.e.* 53 h), the derivative of the mean pattern to accommodate a shift in 2θ, and two time-varying diffraction components that were based on rotation of the principal-component loading vectors. The abundances of the latter two components were constrained to fall in the range from 0 to 1; thus, these represent relative concentrations over the course of the reaction. The abundance of the first component was constrained to be constant in time in order to model the fixed components of the *in situ* cell. The derivative component was kept equal to that of the mean pattern, but its abundance was unconstrained, that is, the 2θ shift could occur in either direction. All calculations were performed with *MATLAB* (The Mathworks, 2006) using constrained least-squares routines that were developed in-house (Van Benthem *et al.*, 2002; Van Benthem & Keenan, 2004). A total of 100 iterations were required for convergence to the final components. Discussion of the resulting MCR–ALS components follows.

4. Results and discussion

In spite of the challenges associated with the complicated *in situ* XRD patterns as illustrated in Fig. 1(*b*), there are significant advantages to performing this type of experiment. Obtaining a picture of the entire discharge of a functioning battery from a structural perspective holds great promise for obtaining a better understanding of structure/property relationships. This is because the observed structural changes within the cell are tied directly to the electrochemical behavior. In addition, the data are collected in real-time, so every diffraction pattern can be compared 'in-context' with the other patterns collected in the same series. This helps in the analysis of subtle changes occurring during the experiment, a luxury that *ex situ* analysis techniques find much more difficult to demonstrate.

4.1. Overview comparison of electrochemical/*in situ* XRD results

Fig. 4 shows the voltage *versus* time discharge plot for the *in situ* cell along with the estimated fraction of spent cell capacity. This plot shows the typical voltage drop during the beginning of the discharge cycle (within the first 20 min) as well as the plateau region ~2.6 V which persists until ~50 h. This is followed by the failure of the cell at ~54 h as illustrated by the fast voltage drop down to below 1.5 V. Such behavior is typical for $(CF_x)_n$ and similar discharge curves have been observed on similar capacity *t*-cells. It is worth noting here that the cell was discharged at a rate of C/72 but displayed full discharge after ~55 h instead of the expected 72 h. This is likely a result of an overestimation of the total capacity for the cell based on our fabrication or could also result from a breakdown in the electrochemical cell due to possible de-lamination. Regardless, we were still able to monitor the reaction process *in situ*, for the purposes of detecting the electrochemical reaction therein. Fig. 5 shows the entire X-ray diffraction data set collected during the *in situ* XRD analysis. At first glance, the

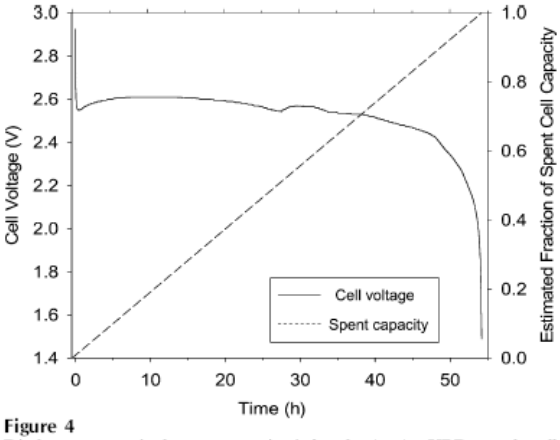

Figure 4
Discharge curve (voltage *versus* time) for the *in situ* XRD pouch cell along with the estimated fraction of spent cell capacity.

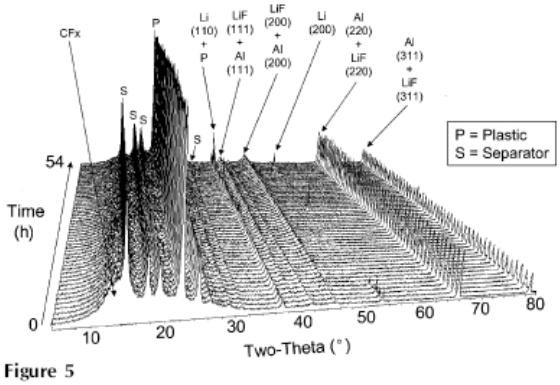

Figure 5
XRD results for *in situ* discharge of the $(CF_x)_n$ pouch cell.

patterns do not appear to change very much. Upon looking closer at the series of patterns, the *in situ* XRD data set reveals peaks matching the LiF phase. Detectable LiF signal first appears early on in the discharge process (within the first 10 h) and the signal increases as the pouch cell is discharged. However, an additional difficulty regarding the *in situ* XRD data is that the diffraction pattern for LiF is almost identical to that of aluminium metal owing to their similar symmetry (f.c.c.) and unit-cell dimensions: a = 4.027 Å for LiF and a = 4.049 Å for aluminium. Hence LiF diffraction peaks almost exactly overlap the locations of Al peaks from the cathode current collector. This news is not all bad because the Al shows considerable texture that exaggerates its 220 and 311 peaks while simultaneously reducing the 111 and 200 peaks to near background, as noted earlier in Fig. 1(*b*). The strong Al 220 and 311 peaks do conceal the LiF 220 and 311 intensities as the LiF phase develops during discharge. Fortunately, the $\sin(\theta)$ dependence of the XRD measurement begins to separate the peak locations for LiF and Al at higher 2θ angles owing to the small difference in lattice parameters for the two materials. Even with this benefit, analysis of the XRD data proved very difficult. The main $(CF_x)_n$ peak appeared to reduce during the discharge process, but it was hard to quantify owing to the severe overlap with the separator peaks. Hence we pursued the mathematical analysis of these data using MVA.

4.2. Li peak removal

Before discussing the MVA results, completeness necessitates that we address the issue of the Li metal anode. As one can see from Fig. 5, Li metal peaks appear as strong intensity spikes in some XRD scans but are absent in others. This is an artifact resulting from the very large grain size of the Li metal anode. These large Li grains (> 100 µm) will strongly diffract X-rays but only if the Li grain is perfectly aligned. The very slight movement of the pouch cell during discharge (due to the dynamic nature of the *in situ* analysis) appears to have brought a few of these grains into the diffraction condition. This condition is temporary though, as one can see such peaks come and go throughout the scan series. These variations hamper the MVA by greatly increasing the number of components observed. As these Li peaks can easily be attributed to experimental artifact, the small 2θ regions where these peaks were observed were removed from the data set prior to MVA analysis.

4.3. MCR–ALS component analysis

4.3.1. Inert components. With the above qualification noted, the initial PCA analysis revealed a four-component system for the XRD data set and this number was used for the subsequent MCR–ALS analysis. We have already outlined the initial PCA analysis (Fig. 3). We now discuss the MCR–ALS results; these results are easier to interpret with respect to an actual physical basis. Components from the MCR–ALS analysis shall be designated by the prefix abbreviation 'Cmpt' for clarity so as to not be confused with the initial PCA results. The MCR–ALS components and their behavior with time (*i.e.* discharge) are compiled in Figs. 6–9. Figs. 6(*a*)–9(*a*), plotted as intensity *versus* 2θ, represent the individual features of the XRD data that vary together systematically. Recombination of these components in the proper proportions based on their magnitude will essentially produce a de-noised version of the observed data set. Note that Figs. 6(*b*)–9(*b*) plot the time-varying magnitude of each component as relative abundance. With this choice of normalization, the contribution of each component to the overall signal level is captured by the corresponding diffraction profile. It is clear from Figs. 6(*a*)–9(*a*) that the first component (Cmpt-1), as seen in Fig. 6(*a*), has the largest overall scale (in counts) and the overall intensity (in counts) decreases for subsequent components (Figs. 7*a*–9*a*).

Fig. 6(*a*) displays Cmpt-1 and is easily recognized as the diffraction signal from all the constituent parts of the pouch cell along with observable intensity from the LiF product. The presence of LiF in this component is dictated by our choice of abundance normalization; that is, we are forced to subtract decreasing amounts of LiF signal from its maximum intensity

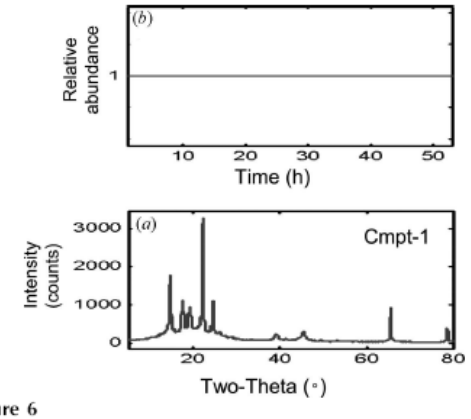

Figure 6
MCR–ALS results: (*a*) component 1 representing an estimate of the final state of the cell; (*b*) relative abundance (constrained to unity).

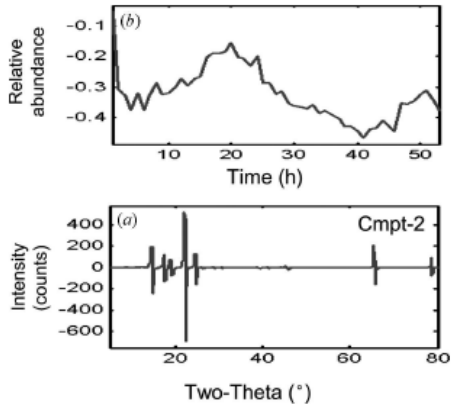

Figure 7
MCR–ALS results: (*a*) component 2 representing the subtle shifting (*i.e.* displacement of the cell) during discharge; (*b*) relative abundance.

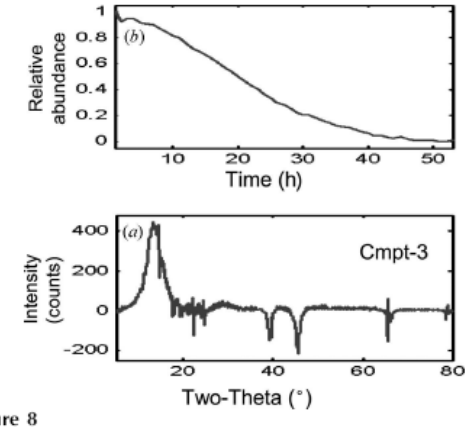

Figure 8
MCR–ALS results: (*a*) component 3 representing the inversely coupled relationship of $(CF_x)_n$ and LiF during discharge; (*b*) relative abundance.

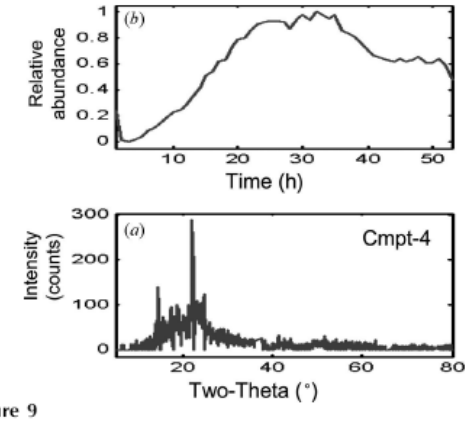

Figure 9
MCR–ALS results: (*a*) component 4 indicative of an additional weak component possibly associated with an intermediate phase; (*b*) relative abundance.

rather than adding increasing amounts of LiF intensity to the background. Our rationale for fixing the relative abundance of Cmpt-1 in the MCR–ALS analysis was a direct result of the observations from the initial PCA analysis, namely, that a large portion of the diffraction signal could be attributed to a diffraction signature that remains unchanged with time and is associated with many of the inert parts of the pouch cell. If we disregard the LiF signal in Cmpt-1, the remaining intensity indeed matches the scattered intensity from the inert parts of the pouch cell (*i.e.* the plastic, separator and aluminium peaks). The second component (Cmpt-2), shown in Fig. 7(*a*), accounts for the slight shifting nature of the pouch cell owing to the dynamic nature of the experiment. The net effect of the specimen shift results in changes in peak intensity over small 2θ angles about the average peak locations for Cmpt-1 and, therefore, results in the derivative-like appearance of Fig. 7(*a*). The overall shift of Cmpt-2 is estimated to be ~75 µm total specimen displacement. Cmpt-1 (minus the LiF signal) and Cmpt-2 taken together with their respective magnitudes shall hereafter be referred to as the 'inert-component' (I-Cmpt) of the MCR–ALS analysis.

4.3.2. Dynamic components. Fig. 8(*a*) shows the third component (Cmpt-3). The positive intensity looks very similar to the signal from $(CF_x)_n$ as shown in Fig. 1(*a*) [note that the strong peak ~13° 2θ along with a weaker peak ~26° 2θ are consistent with the 001 and 002 $(CF_x)_n$ reflections, respectively]. Superimposed on this $(CF_x)_n$ pattern, but with opposite sign, is the intensity associated with the LiF phase. The magnitude of Cmpt-3 (Fig. 8*b*) decays with time as discharge progresses. By grouping them together, Cmpt-3 is clearly showing the inverse relationship between the $(CF_x)_n$ and LiF intensities. To interpret this component properly, one can think of the decay of negative LiF intensity with cell discharge as, in fact, the formation of the LiF phase as $(CF_x)_n$ decomposes.

As with all of these MVA techniques, the analysis is prone to some mixing of components. Such MVA artifacts can be

observed in Fig. 8(*a*) as spikes of negative or positive intensity that have unrealistically thin peak widths. They occur because of incomplete modeling of the I-Cmpt. The intensity spikes located at ~14.5, ~18, ~19.2 and ~24.6° 2θ in Fig. 8(*a*) are associated with separator peaks from the I-Cmpt. The sharp spike ~22.2° 2θ in Fig. 8(*a*) is associated with the strong plastic peak from the I-Cmpt and the intensity spike ~65.6° 2θ is associated with the Al 311 peak of the I-Cmpt.

Fig. 9 shows the fourth component (Cmpt-4) derived from the MCR–ALS analysis. Its scale is low (Fig. 9*a*) and so it is considered the most subtle component of the discharge process. This component also suffers from some component mixing as it shows a few spikes of intensity associated with the separator and plastic peaks. Overall though, it appears to be stable within the MCR–ALS solution and so is considered potentially significant. Ignoring the intensity spikes, the overall component looks like a broad amorphous peak centered about ~23° 2θ. If one considers the magnitude of the signal (Fig. 7*b*), Cmpt-4 appears to increase in magnitude (*i.e.* relative abundance) during the initial discharge process, maximizes at roughly the half-way point of discharge, and then shows a small decay of abundance as the completion of the discharge approaches. It appears that the intensity of this component is in some way associated with an intermediate phase that forms during $(CF_x)_n$ decomposition. It is also worth noting that the intensity of Cmpt-4 does not completely decay after reaching its peak abundance (at ~25–35 h), but persists as a plateau of abundance (~41–50 h) until the conclusion of the cell discharge. Recently, $(CF_x)_n$ cathodes fabricated using a low-temperature fluorination process (Guerin *et al.*, 2006) have been analyzed. This cathode material, denoted as CF(LT)-300N2 (Guerin *et al.*, 2006), showed similar broad peaks in the 15–30° 2θ range. One of these broad XRD peaks, observed at a higher than 20% depth of charge, was identified as an intercalation compound CF(x–y)-Li^+. Guerin *et al.* (2006) noted that, once formed, this phase persisted throughout the remainder of the discharge process. This phase, observed by Guerin *et al.* (2006) in their *ex situ* XRD analysis of CF(LT)-300N2 cathodes at various states of discharge, has also been speculated to exist for $(CF_x)_n$ compounds synthesized using a higher-temperature process (Touhara *et al.*, 1984; Hagiwara *et al.*, 1988). However, evidence for the existence of the intercalation compound CF(x–y)-Li^+ has been elusive for materials prepared *via* the higher-temperature processing (Guerin *et al.*, 2006; Hagiwara *et al.*, 1988; Touhara *et al.*, 1984). Our use of *in situ* XRD analysis (coupled with the application of MCR–ALS) suggests evidence for the CF(x–y)-Li^+ phase in the discharge process of our *in situ* pouch cell. Our analysis suggests that this intermediate phase undergoes only limited decomposition (*i.e.* breakdown) as the reaction progresses toward cell failure. This is suggested by the fact that the abundance for Cmpt-4 (Fig. 7*b*) does not decay to zero but appears to level out in concentration after ~40 h of discharge. In this sense, the CF(x–y)-Li^+ phase is an intermediate phase only in terms of its maximum abundance at the midpoint of discharge (~25–30 h). A true intermediate phase would completely decompose by the conclusion of the reaction.

4.4. Contour map comparison

Fig. 10 shows a comparison of the collected XRD data as contour plots (Figs. 10*a* and 10*b*) along with the corresponding electrochemical behavior of the cell (Fig. 10*c*). Both of the

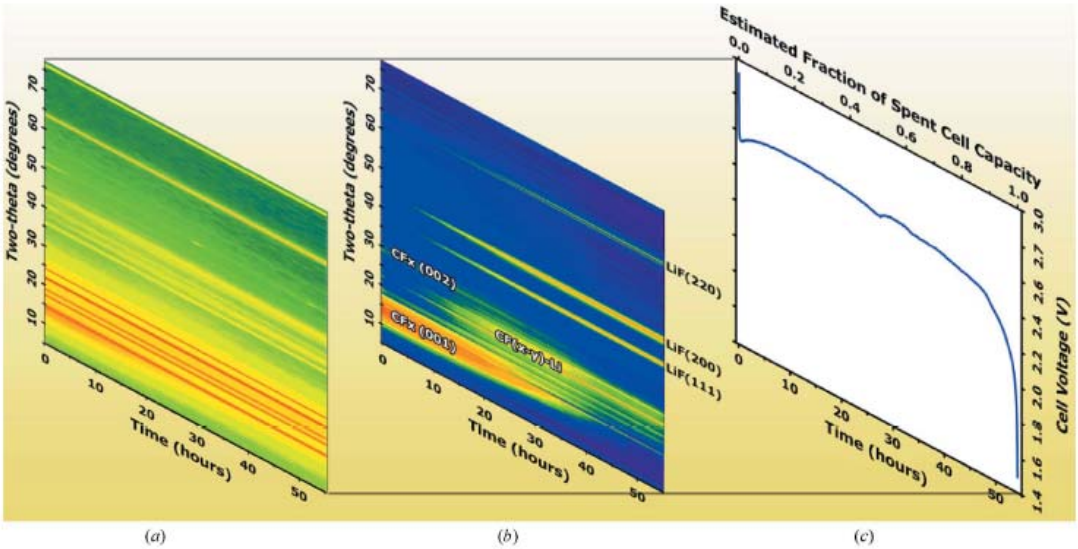

Figure 10
Log-scale contour plots for the XRD data set (*a*) as collected and (*b*) regenerated from the abundance-weighted sums of Cmpt-3 and Cmpt-4 (*i.e.* removal of the I-Cmpt). Color (rainbow spectrum) denotes magnitude of intensity (blue = low intensity, red = high intensity). Discharge curve (*c*) shows correlated electrochemical properties as a function of the discharge process.

contour plots have been graphed using a log scale to enhance weak features of the discharge sequence. Fig. 10(*a*) shows what the raw XRD data looks like before MCR–ALS analysis. This plot shows the presence of many peaks (long streaks) due to the plastic, separator, lithium and aluminium (red/orange colors indicate regions of high intensity, green areas indicate background level). However, it is possible to detect the subtle effects of the $(CF_x)_n$ and LiF peaks as weak intensity near the background. In contrast, Fig. 10(*b*) shows the superimposed (summed) patterns for Cmpt-3 and Cmpt-4. In fact, the data in Fig. 10(*b*) have been plotted in such a way as to generate positive intensity for the LiF signal in correct proportion to its magnitude during the discharge process. Note that high intensity is denoted by the red/orange colors and low intensity (background) is shown in blue in Fig. 10(*b*). This plot definitively illustrates the decay of $(CF_x)_n$ along with the formation and growth of LiF during discharge. It also more clearly shows the formation of the possible CF(x–y)-Li^+ intercalation phase as a broad intensity distribution in the 20–25° 2θ range with increasing intensity during electrochemical discharge, up until about hour 35; this can be detected by the progressive blue-to-green-to-yellow contours observed in the 20–25° 2θ range, which indicate increased counts. At approximately 35 h, the intensity begins to decrease slightly in signal as the color again reverts to a green contour. However, the overall presence of the CF(x–y)-Li^+ intercalation phase persists until the conclusion of the discharge process, as the intensity in this 20–25° 2θ range does not return to background (*i.e.* blue contour level).

It can be tempting to over-interpret such MVA results. What we can definitively say regarding our *in situ* XRD analysis is that we observe $(CF_x)_n$ intensity decay that is coupled to LiF phase formation during discharge, and that MCR–ALS works adequately to remove the convoluted intensity associated with the inert constituents of the pouch cell that tend to dominate and obstruct the dynamic portion of the XRD data. The removal of I-Cmpt significantly enhances the quality and quantifiability of the analysis, and even hints at subtleties such as a possible additional component of the reaction process [for example CF(x–y)-Li^+].

5. Conclusions and outlook

We have successfully investigated the discharge process of a Li/$(CF_x)_n$ electrochemical cell by *in situ* XRD. Mathematical treatment of the XRD data set using an alternating least-squares-based multivariate curve resolution (MCR–ALS) technique successfully separated the convoluted XRD signal. The resulting components could be separated and easily assigned as inert components (I-Cmpt) and dynamic components, thereby isolating the intensity due to the chemical reaction from the superimposed scatter associated with the dominant I-Cmpt. One of the resulting dynamic components revealed an inverse correlation between the $(CF_x)_n$ cathode signal and the LiF by-product intensity. Furthermore, we observed an additional dynamic component, which may be associated with the formation of an intermediate compound during the discharge process. The application of multivariate statistical analysis (MVA) to XRD data is an exciting development and is likely to play an increasingly significant role with regard to future analysis of large multidimensional data sets common to *in situ* experiments.

The authors thank Bryan Sanchez for preparation of the pouch cell. MAR thanks Colleen S. Frazer and Kathy Rice for their aid in generating the color contour maps presented herein. Sandia is a multiprogram laboratory operated by Sandia Corporation, a Lockheed Martin Company, for the United States Department of Energy under contract DE-AC04-94AL85000.

References

Chartouni, D. & Gross, K. (2001). *J. Electrochem. Soc.* **148**, A241–A248.
Chen, Z. P., Morris, J., Martin, E., Hammond, R. B., Lai, X., Ma, C., Purba, E., Roberts, K. J. & Bytheway, R. (2005). *Anal. Chem.* **77**, 6563–6570.
Guerin, K., Dubois, M. & Hamwi, A. (2006). *J. Phys. Chem. Solids*, **67**, 1173–1177.
Hagiwara, R., Nakajima, T. & Watanabe, N. (1988). *J. Electrochem. Soc.* **135**, 2128–2133.
Harman, H. H. (1976). *Modern Factor Analysis*, 3rd revised ed. The University of Chicago Press.
Hatchard, T. D. & Dahn, J. R. (2004). *J. Electrochem. Soc.* **151**, A838–A842.
Jollife, I. T. (2002). *Principal Component Analysis*, 2nd ed. New York: Springer-Verlag.
Keenan, M. R. & Kotula, P. G. (2004*a*). *Appl. Surf. Sci.* **231–232**, 240–244.
Keenan, M. R. & Kotula, P. G. (2004*b*). *Surf. Interface Anal.* **36**, 203–212.
Kotula, P. G., Keenan, M. R. & Michael, J. R. (2003). *Microsc. Microanal.* **9**, 1–17.
Malinowski, E. R. (1987). *J. Chemometrics*, **1**, 33–40.
Nagasubramanian, G. & Rodriguez, M. A. (2007). *J. Power Sources*, **170**, 179–184.
Reimers, J. N. & Dahn, J. R. (1992). *J. Electrochem. Soc.* **139**, 2091–2097.
Rodriguez, M. A., Ingersoll, D. & Doughty, D. H. (1998). *Mater. Res. Soc. Symp. Proc.* **496**, 275–285.
Rodriguez, M. A., Ingersoll, D. & Doughty, D. H. (2000). *Adv. X-ray Anal.* **42**, 267–273.
Tauler, R., Kowalski, B. & Fleming, S. (1993). *Anal. Chem.* **65**, 2040–2047.
The Mathworks (2006). *MATLAB*. Version 7.3. The Mathworks Inc., Natick, MA, USA.
Touhara, H., Fujimoto, H., Watanabe, N. & Tressaud, A. (1984). *Solid State Ionics*, **14**, 163–170.
Van Benthem, M. H. & Keenan M. R. (2004). *J. Chemometrics*, **18**, 441–450.
Van Benthem, M. H., Keenan, M. R. & Haaland, D. M. (2002). *J. Chemometrics*, **16**, 613–622.
Watanabe, N. (1980). *Solid State Ionics*, **1**, 87–110.
Whittingham, M. S. (1975). *J. Electrochem. Soc.* **122**, 526–527.

Appendix C

Available online at www.sciencedirect.com
ScienceDirect
Journal of Power Sources 170 (2007) 179–184
JOURNAL OF POWER SOURCES
www.elsevier.com/locate/jpowsour

Short communication

Performance enhancement at low temperatures and in situ X-ray analyses of discharge reaction of Li/$(CF_x)_n$ cells

Ganesan Nagasubramanian [a,*], Mark Rodriguez [b]

[a] 2521 Advanced Power Sources Technology Department, Sandia National Laboratories, Albuquerque, NM 87185, United States
[b] 1822 Materials Characterization, Sandia National Laboratories, Albuquerque, NM 87185, United States

Received 8 March 2007; received in revised form 2 April 2007; accepted 3 April 2007
Available online 18 April 2007

Abstract

In the Sandia National Laboratories internally funded Laboratory Directed Research and Development (LDRD) project we are studying the fundamental limitation(s) of the discharge reaction that reduces the operating voltage of the Li/$(CF_x)_n$ cells at moderate discharge rates. As a subset of this effort, we are evaluating the electrochemical properties of $(CF_x)_n$ electrodes prepared with materials from different vendors at different temperatures and in two different electrolytes in order to provide an optimized system to the above study. The temperatures studied span the range −51 to 72 °C. The electrolytes consist of EC:EMC (3:7 wt.%)–1.2 M $LiPF_6$ denoted as HCE (Highly Conductive Electrolyte) and EC:PC:EMC (1:1:3 wt.%)–1 M $LiBF_4$ denoted as SNL-E (Sandia National Laboratories Electrolyte). The four different $(CF_x)_n$ materials studied showed comparable capacity at 0 °C and above in the two electrolytes. However, at sub-ambient temperatures the SNL-E performed better than the HCE. The performance improvement with SNL-E comes mainly from a lower interfacial resistance compared to HCE.

The different $(CF_x)_n$ materials performed differently in the SNL-E especially at sub-zero temperatures. For example, at sub-zero temperatures the delivered capacity varied between 6% and >60% of the room temperature capacity. In order to rationalize this observation, SEM photographs of the powder particles were taken that showed that the particle size of the best performer(s) is smaller than that of the others. Finally, these data seem to indicate that optimization of the properties of the electrolyte as well as the electrode is critical to maximizing delivered capacity especially at sub-ambient temperatures.

Our X-ray results shall be presented in more detail in an upcoming manuscript. We have elected to present a brief discussion of these results in this present paper as the findings lend support to the formation of intermediate species in the discharge reaction of Li/$(CF_x)_n$ cell.
Published by Elsevier B.V.

Keywords: Carbon monofluoride; Impedance; PVDF; Interfacial resistance

1. Introduction

Lately there is growing interest in improving the performance of Li/$(CF_x)_n$ cells for space and military applications. Of all the known ambient temperature Li-primary chemistries Li/$(CF_x)_n$ has the highest theoretical specific capacity and energy (vide infra Table 1). The theoretical specific energy and capacity are for $x = 1$ (each carbon has one F attached). However, the practical energy is only 10–35% of the theoretical depending on the discharge rate and cell size. One of the reasons for the poor performance may be coming from low operating cell voltage (~2.5 V) which is much lower than the OCV of ~3.4 V. In general, there seems to be a consensus in the scientific community that an intermediate species (in the discharge reaction) is responsible for the depression in the operating voltage. During the 1970s and 1980s several researchers proposed reaction schemes but without irrefutable proof for their hypotheses. For example, Hagiwara et al. [1] based on their analyses of discharge products and OCV measurements in different solvents proposed that the discharge reaction includes electrochemical formation of an intermediate phase comprising of Li^+, (CF) and solvent molecule and the subsequent chemical decomposition of the intermediate to the final products. However, there was no proof for the existence of the intermediate species. Whittingham et al. [2] proposed that a ternary non-stoichiometric intercalation compound of the type $(CLi_xF)_{x<1}$ formed in the discharge reaction determined the OCV of the cell. He also suggested that when (CF_x) is chemically reduced its inter-planer spacing

* Corresponding author. Tel.: +1 505 844 4684; fax: +1 505 844 6972.
E-mail address: gnagasu@sandia.gov (G. Nagasubramanian).

0378-7753/$ – see front matter. Published by Elsevier B.V.
doi:10.1016/j.jpowsour.2007.04.023

Table 1
Comparison of the electrochemical properties of li primary cells

Chemistry	Voltage (v)	Specific energy (Wh kg^{-1})		% theoretical
		Theoretical	Practical	
Li/MNO_2	3.0	1005	200–270	
Li/SO_2	3.0	1170	240	
Li/$SOCl_2$	3.6	1470	430	∼30
Li/$(CF_x)_n$	3.2	2260	220	∼10

expands to 9.35 Å. However, this type of lattice expansion could not be confirmed in an electrochemically reduced material.

At Sandia National Laboratories we are working on an LDRD program aimed at understanding the discharge reaction mechanism to propose solution(s) for increasing the operating voltage close to 3.0 V at moderate discharge rates. In the LDRD effort we will be using techniques such as TOFSIMS (Time of Flight Secondary Ion Mass Spectroscopy), STM (Scanning Tunneling Microscopy), etc., to look at directly the discharge mechanism. This work will be published elsewhere. As a subset of this effort we are looking at $(CF_x)_n$ materials from different sources to select the best material (for capacity) for the above study. In this paper we describe the electrochemical data on Sandia-built Li/$(CF_x)_n$ coin cells and compare performance especially at low temperatures in two different electrolytes.

We have developed a method for in situ XRD analysis of "pouch" cells for the purposes of obtaining information on the structure/property relationships regarding battery systems [3,4]. In the pouch technique, a functional cell (cathode, separator, anode, electrolyte, etc.) is assembled within a very thin plastic baggie, and then vacuum-sealed in such a way as to allow the electrode leads to exit the sealed pouch. Sufficient penetration of X-rays through the low-*Z* materials that make up the pouch cell allows scrutiny of structural changes occurring within the anode and/or cathode as the functional cell is discharged. We employed this technique to analyze the $(CF_x)_n$ cathode material as a function of discharge.

2. Experimental

Four different $(CF_x)_n$ cathode materials were purchased from three vendors. The different materials are denoted as $(CF_x)_n$-1; $(CF_x)_n$-2; $(CF_x)_n$-3; $(CF_x)_n$-4. $(CF_x)_n$-3 and $(CF_x)_n$-4 were purchased from the same vendor. These materials differ in % fluorine content and in particle size (see below SEM photographs). The value of x in these materials is

$(CF_x)_n$-1; $x =: 0.8 - 1.2$; $(CF_x)_n$-2; $x =: 1.02$;

$(CF_x)_n$-3; $x =: 1.0$ and $(CF_x)_n$-4; $x =: 0.9 - 1.0$

The average particle size of $(CF_x)_n$-1 is ∼8 μm, that of $(CF_x)_n$-2 is around 5–6 μm and that of $(CF_x)_n$-3 and $(CF_x)_n$-4 is around 4 μm. Kureha PVDF was used as binder along with carbon (Gulf Shawinigan Acetylene Black) for improving the electronic conductivity of the electrode. These materials were vacuum baked at 100 °C overnight before using. The battery grade solvents ethylene carbonate (EC); propylene carbonate (PC); ethyl methyl carbonate (EMC) purchased from Mitsubishi Chemicals (Japan) were used as received. The lithium salts ($LiPF_6$ and $LiBF_4$) purchased from Hashimoto, were vacuum dried at 60 °C overnight before using.

2.1. Electrode making

PVDF is dissolved in NMP followed by the addition of carbon. This mixture is stirred to disperse carbon uniformly before adding the $(CF_x)_n$ powder. This mixture is stirred for an hour before making electrodes. This mixture is a slurry with an aggregate particle size of ∼3–5 μm and with a typical composition of 5 wt.% each of the PVDF and carbon and 90 wt.% $(CF_x)_n$. This is coated on to a carbon coated (3 μm thick) aluminum current collector (∼12 μm thick) in a Hohsen coater model # HSCS-200. The typical thickness of the dried electrode is ∼72 μm. In a typical coating run several meters-long electrodes were prepared. The electrodes are baked in vacuum at 100 °C overnight before testing them in coin cells.

Electrodes (∼2 cm^2 area) for the coin cells (2032 size; 2 cm diameter and 0.032 cm thick) were punched from these large electrodes.

Two different electrolytes were used in our study. The compositions of the electrolytes are given below—Highly Conductive Electrolyte (HCE): EC:EMC (3:7 wt.%)–1.2 M $LiPF_6$; Sandia Electrolyte (SNL-E): EC:PC:EMC (1:1:3 wt.%)–1 M $LiBF_4$.

The ionic conductivity of HCE is ∼10 mS cm^{-1} around room temperature and that of SNL-E is ∼4–5 mS cm^{-1}. HCE exhibited higher ionic conductivity at all temperatures investigated in this study. Several coin cells with Sandia-coated electrodes were prepared containing these electrolytes. A suite of electrochemical measurements including impedance and discharge at different temperatures were performed to characterize cell behavior.

2.2. Impedance measurement

Impedance measurements were carried out in three-electrode configuration in T-Cells at a couple of different temperatures. The three-electrode configuration allows the measurement of the full cell, cathode and anode impedances. The Solatron impedance equipment consisting of SI 1287 Electrochemical Interface and 1255B Frequency Response Analyzer controlled with Zplot was used for impedance studies. The cell impedance was measured between 100 kHz and 100 mHz. A minimum of two cells were studied for each-chemistry and the cell-average was plotted in Figs. 6 and 7.

3. Results and discussion

3.1. Discharge studies

SNL-built coin cells were used for the studies. The cells were discharged in a Maccor tester model # Series 4000. A typical discharge curve for one of the $(CF_x)_n$-3 cells is given in Fig. 1. The cell was discharged at a C/200 rate and 25 °C. The voltage

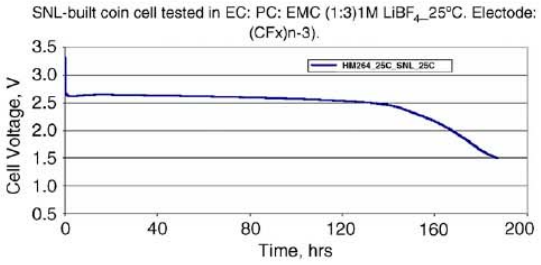

Fig. 1. Voltage response of a Sandia-built coin cell for a C/200 discharge rate at 25 °C.

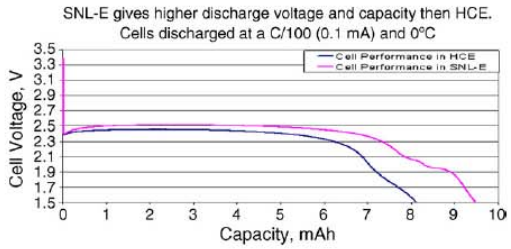

Fig. 2. Cell voltage vs. delivered capacity at a C/100 rate (0.1 mA) and 0 °C.

dropped initially and remained nearly flat for all most 100 h before starting to decrease. Similar behavior was observed for the other materials.

Even at a C/200 rate the operating voltage is only around 2.6 V which is about 0.6–0.8 V lower than the OCV. The measured capacity of the cell is ~9 mAh which is 99% of the theoretical capacity based on the weight of the cathode active material in the cell. Similar tests were performed at different temperatures for the four different $(CF_x)_n$ materials.

In Figs. 2 and 3 are compared the discharge curves for the two electrolytes at two rates and 0 °C. At C/100 and C/5 rates the SNL-E gave higher operating voltage and capacity than the HCE. At C/5 the improvement in performance with SNL-E is higher than at C/100.

In Fig. 4 are compared the discharge capacity for the $(CF_x)_n$-1 in the two electrolytes at different discharge rates.

The solid curves are for the HCE containing cells and the dashed lines are for the SNL-E containing cells. The delivered capacities at C/5; C/50; C/100 and C/200 rates and at tempera-

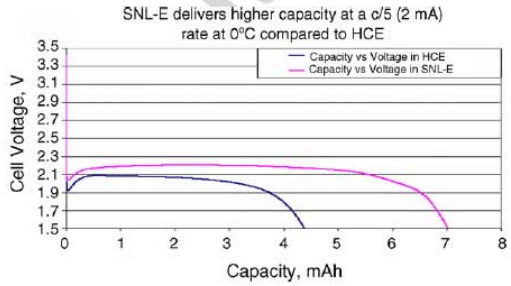

Fig. 3. Cell voltage vs. delivered capacity at a C/5 rate (2 mA) and 0 °C.

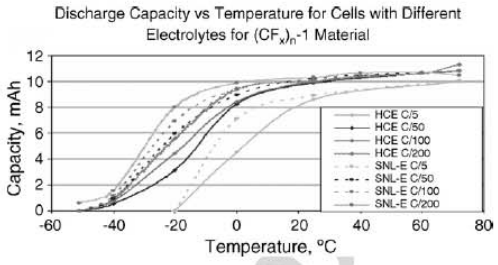

Fig. 4. Discharge capacity vs. temperature for the $(CF_x)_n$-1 material in the two electrolytes.

tures in the range −51 to 72 °C are compared. The plots clearly show that the performance of SNL-E containing cells in general is better than the HCE containing cells especially at sub-ambient temperatures. In general, this behavior is true for the other $(CF_x)_n$ materials investigated in this study. For example, the behavior of $(CF_x)_n$-2 is similar to $(CF_x)_n$-1 as shown in Fig. 5. The other two materials also showed improved performance in SNL-E. However, we tested them only at a couple of temperatures.

Although HCE has higher ionic conductivity than the SNL-E the electrochemical performance of the SNL-E is superior. Obviously the trend in the ionic conductivity cannot explain this observation. The observed performance can be explained by the interfacial resistance. This is explained in the next section.

3.2. Effect of interfacial resistance on performance

In Figs. 6 and 7 are shown NyQuist plots of impedance at 25 °C and −20 °C respectively for the cathode at the same cathode voltage (2.9 V) in the two electrolytes. For each cell, at temperature, the full-cell, cathode and anode impedances were measured. Over 90% of the full-cell impedance comes from the cathode. Since the cathode contributes to majority of cell impedance, only the cathode impedances are compared. These plots indicate clearly that the interfacial resistance of cathode in SNL-E is lower than the HCE. However, the cell with SNL-E shows higher ohmic (high-frequency) resistance than the HCE electrolyte. In Fig. 6B are shown expanded view of the NyQuist plots. There are two arcs at the higher frequencies seen for SNL-E. However, the arcs are convoluted for the HCE. Others have seen two arcs for $LiCoO_2$ cathode [5]. Since it is not the intent

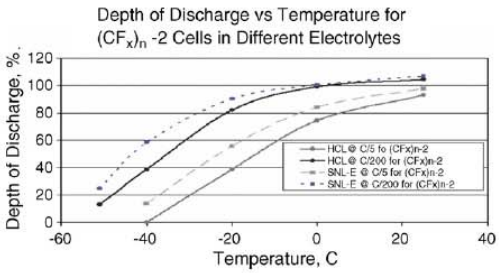

Fig. 5. % discharge capacity vs. temperature for the $(CF_x)_n$-2 material in the two electrolytes.

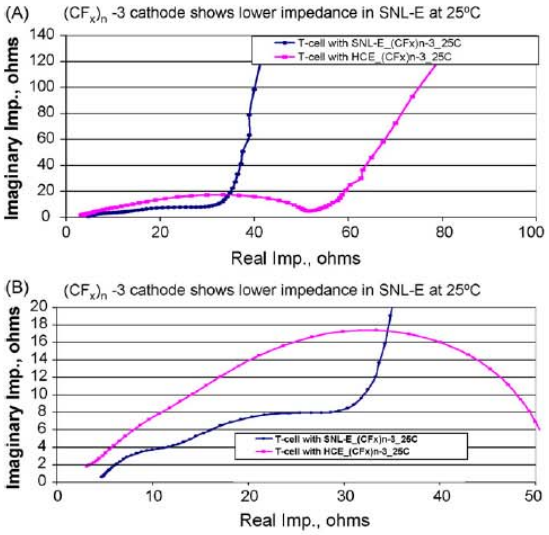

Fig. 6. (A) NyQuist plot of impedance for $(CF_x)_n$-3 at 25 °C in the two electrolytes. (B) Expanded view of NyQuist plot of impedance for $(CF_x)_n$-3 at 25 °C in the two electrolytes.

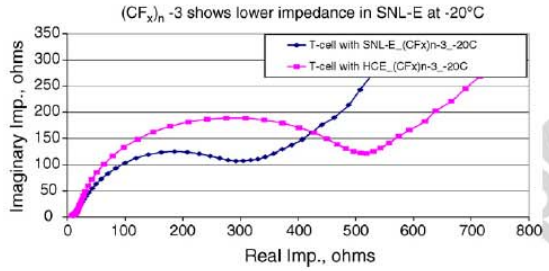

Fig. 7. NyQuist plot of impedance for $(CF_x)_n$-3 at −20 °C in the two electrolytes.

of this paper to critically analyze the impedance data, but to show that electrolytes with lower cathode/electrolyte interfacial resistance performs better, the readers are referred to Ref. [5] for analyses for a similar data. At −20 °C the difference in interfacial resistance is much more dramatic than at 25 °C which implies that HCE should perform progressively worse at sub-ambient temperatures than the SNL-E. This observation clearly suggests that it is not sufficient to increase the ionic conductivity of the electrolyte but improve the electrode/electrolyte interfacial resistance. Similar observation has been reported by

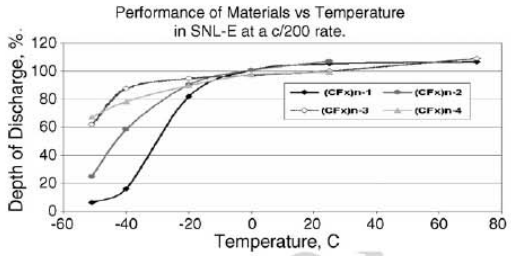

Fig. 8. Performance of the $(CF_x)_n$ materials in SNL-E at different temperatures at a C/200 rate.

Table 3
% discharge capacity at different sub-ambient temperatures

Temperature (°C)	$(CF_x)_n$-1	$(CF_x)_n$-2	$(CF_x)_n$-3	$(CF_x)_n$-4
−20	82	82	95	90
−40	16	39	88	82
−51	6	25	62	67

Tested in SNL-E and at a C/200 rate.

others for Li-ion cells [6]. In Table 2 are given the ohmic and the total cell resistances culled from the impedance plots for cells containing the two electrolytes. At both temperatures the cathode showed lower cell impedance in the SNL-E compared to HCE. We also performed three-electrode impedance measurements on the $(CF_x)_n$-1 and $(CF_x)_n$-2 cathodes and observed similar electrolyte behavior.

Based on the above observation we continued our investigation on the other materials mainly in SNL-E. In Fig. 8 are compared the discharge capacities for the four different materials in SNL-E at different temperatures. In Table 3 the performance values culled from Fig. 8 are given.

The performance at a C/200 rate of the different materials is comparable above 0 °C. However, the performance at sub-zero temperatures varies significantly. For example, at sub-ambient temperatures the performance of $(CF_x)_n$-3 is better than the rest (except at −51 °C). At −40 °C, while $(CF_x)_n$-3 gave ∼88% of the capacity $(CF_x)_n$-1 gave only 16%. At −51 °C the performance of $(CF_x)_n$-3 is very nearly comparable or slightly lower to that of the $(CF_x)_n$-4.

In this study we used the SNL-E which showed best electrochemical properties. However, the discharge capacity was different for the different materials. Probably the difference has come from the particle size of the material. We took SEM photos of the (CF_x) powders to see if they have different particle sizes. The SEM photos for the four materials are shown below.

Table 2
Impedance values for the coin cells with the two electrolytes

Temperature (°C)	HCE			SNL-E		
	Ohmic (Ω)	Total (Ω)	(Total-ohmic)[a]	Ohmic (Ω)	Total (Ω)	(Total-ohmic)[a]
25	3	79	76	5	41	36
−20	7	746	739	10	526	516

[a] Ohmic resistance subtracted from the total resistance. The total and the ohmic resistances are taken at 100 mHz and 100 kHz, respectively, corresponding to the lowest and the highest frequencies cell impedance was measured at.

The photos of the four (CF_x) powders show that the powder particles have different particle sizes. For example, at 20 μm magnification the particle size decreases in the following order: $(CF_x)_n$-1 > $(CF_x)_n$-2 > $(CF_x)_n$-3 ~ $(CF_x)_n$-4. Materials with smaller particle size perform better. Finally, this observation also emphasizes that both the electrode and the electrolyte properties should be optimized to maximize cell performance.

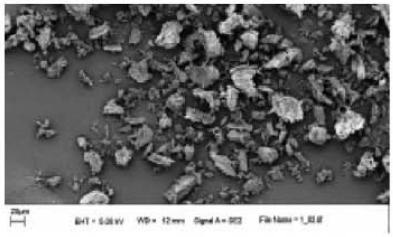

Photo of (CF_x)-1

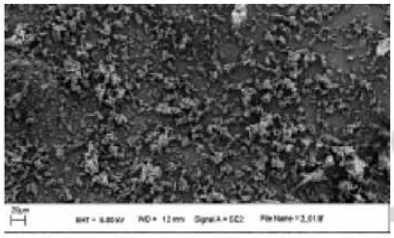

Photo of (CF_x)-2

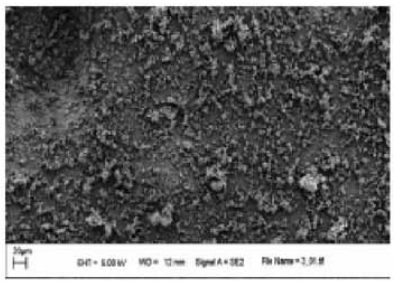

Photo of (CF_x)-3

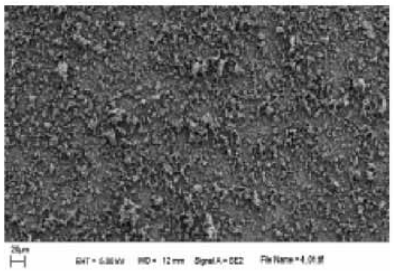

Photo of (CF_x)-4

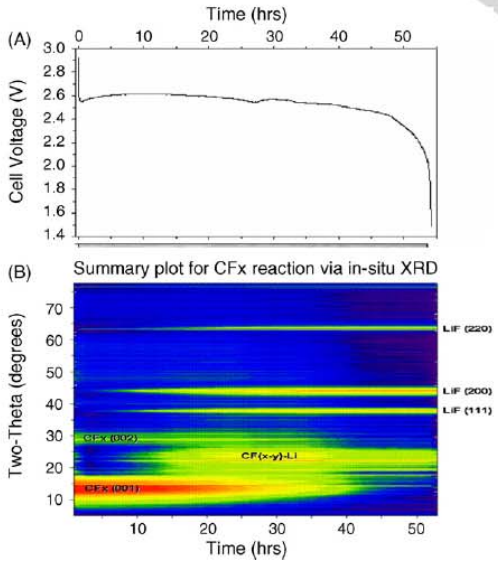

Fig. 9. (A) Discharge curve for our pouch cell, along with a contour plot of the XRD data collected during discharge. (B) A contour plot of the XRD data collected during discharge.

3.3. X-ray studies

Fig. 9A and B shows a summary plot of both the voltage curve obtained during discharge of our pouch cell, along with a contour plot of the XRD data collected using a Siemens D500 θ–θ diffractometer (Cu Kα, λ = 1.5406 Å).

The voltage curve shows typical discharge behavior for $(CF_x)_n$, with a precipitous drop from OCV at the onset of the discharge process, to a plateau voltage of ~2.6 V. This plateau voltage persists until the onset of cell failure. The XRD analysis is shown below the voltage curve as a contour plot, having axes of x = time, and $y = 2\theta$ angle and the intensity (as a log scale) shown as a color scale. The contour plot shows significant presence of the $(CF_x)_n$ cathode material at the beginning of cell discharge as illustrated by the prominent $(CF_x)_n$ (0 0 1) intensity at ~10° 2θ. The contour plot shows the $(CF_x)_n$ intensity dissipating as the cell progresses through discharge. LiF peaks are observed to mature concurrent with the decay of the $(CF_x)_n$ intensity. These observations are consistent with other published results [7–9]. A thorough analysis of the XRD data using multivariate analysis (MVA) cleanly separated the $(CF_x)_n$ feature from scattered intensity due to the fixed components of the pouch cell (e.g. separator). Moreover, the MVA technique suggested that another species, perhaps an intermediate phase, formed during cell discharge as well shown in the contour map as $CF_{(x-y)}$-Li. An in-depth discussion regarding these observations, along with further detail regarding MVA of the obtained XRD dataset is in preparation and shall be presented soon.

4. Conclusions

We tested four different $(CF_x)_n$ materials in two different electrolytes namely HCE and SNL-E. Although HCE showed higher ionic conductivity, its performance was inferior to that of the SNL-E especially at sub-ambient temperatures. Our impedance data showed that SNL-E exhibited lower interfacial resistance than the HCE electrolyte. This observation highlights the importance of lowering interfacial resistance to improving performance. Among the four different materials investigated, $(CF_x)_n$-4 which has the smallest particle showed improved performance. Our work highlights the importance of improving both the electrode and electrolyte properties for increasing performance.

We performed in situ X-ray on pouch cells during discharge and the X-ray data was analyzed using MVA. The MVA analysis strongly suggests the formation of an intermediate species.

Acknowledgments

Sandia is a multi-program laboratory operated by Sandia Corporation, a Lockheed Martin Company, for the United States Department of Energy's National Nuclear Security Administration under contract DE-AC04-94AL85000. The authors would like to thank the Laboratory Directed Research and Development (LDRD) program for funding this work. The authors would also like to thank Lorie Davis for preparing and testing cells.

References

[1] R. Hagiwara, T. Nakajima, N. Watanabe, J. Electrochem. Soc. 135 (1988) 2128.
[2] M.S. Whittingham, J. Electrochem. Soc. 122 (1975) 526.
[3] M.A. Rodriguez, D. Ingersoll, D.H. Doughty, In situ X-ray characterization of $LiMn_2O_4$: a comparison of structural and electrochemical behavior, Mater. Res. Soc. Symp. Proc. 496 (1998) 275–285.
[4] M.A. Rodriguez, D. Ingersoll, D.H. Doughty, An electrochemical cell for in-situ X-ray characterization, Adv. X-ray Anal. 42 (2000) 267–275.
[5] M.G.S.R. Thomas, P.G. Bruce, J.B. Goodenough, J. Electrochem. Soc. 132 (1985) 1521.
[6] T.R. Jow, M.S. Dinga, K. Xua, S.S. Zhanga, J.L. Allena, K. Amine, G.L. Henriksen, J. Power Sources 119 (2003) 343.
[7] K. Guerin, M. Dubois, A. Hamwi, Electrochemical discharge mechanism of fluorinated graphite used as electrode in primary lithium batteries, J. Phys. Chem. Solids 67 (2006) 1173–1177.
[8] H. Touhara, H. Fujimoto, N. Watanabe, A. Tressaud, Discharge reaction mechanism in graphite fluoride-lithium batteries, Solid State Ionics 14 (1984) 163.
[9] R. Hagiwara, T. Nakajima, N. Watanabe, Kinetic study of discharge reaction of lithium-graphite fluoride cell, J. Electrochem. Soc. 135 (1988) 2128.

6. Distribution

Dongwon Shin (1)
Northwestern University
Department of Materials Science and Engineering
633 Clark Street
Evanston, IL 60208

Christopher M. Wolverton (1)
Northwestern University
Department of Materials Science and Engineering
633 Clark Street
Evanston, IL 60208

1	MS0123	Donna L. Chavez	01011
1	MS0614	Cara Johnson	02540
1	MS0614	Thomas F. Wunsch	02546
1	MS0614	Ganesan Nagasubramanian	02546
1	MS1411	Joanne L. Budzien	01814
1	MS0899	Technical Library	09536 (electronic copy)


Sandia National Laboratories